

THE PHOTOELECTROCHEMISTRY OF SOLUTION GROWN ZINC OXIDE NANOWIRE
ARRAYS

Thesis by
Anthony G. Fitch

In Partial Fulfillment of the Requirements

For the Degree of
Doctor of Philosophy

California Institute of Technology

Pasadena, CA

2011

(Defended August 4, 2010)

© 2011

Anthony G. Fitch

All Rights Reserved

ACKNOWLEDGEMENTS

While at Caltech, I had the opportunity to interact with many unique and amazing people, and I appreciate all the help and advice that brought me to this point. The impact of these people and experiences extends far into my professional career and personal life. I have truly benefited from their efforts.

I want to thank Nate Lewis for giving me the opportunity to work in his group on the exciting field of photoelectrochemistry. I have been impressed with his depth of knowledge and I am grateful to have learned from him. His advice and encouragement in times of need were invaluable.

I also want to thank Bruce Brunschwig for all the useful advice, fruitful discussions and support. He has been a great teacher and always made himself available for discussions on research or other issues.

I want to thank the remaining members of my committee, Harry Gray and Mitichio Okumura who are both outstanding scientists and friendly people.

During my years at Caltech, I have worked with many fellow grad students and post docs all of which added to my experience. I want to start with my lab mate Don Walker who has been my partner in crime for my entire time at Caltech. I am grateful for his friendship and all the horizon broadening discussions. I want to thank the scuba crew: Marc Woodka, Craig Wiggenhorn, and Erik Johansson, Team Justice: Edgardo Garcia, Chad Schmutzer, Brian Leigh, Matt Pholman, Jake Wiener and the remaining members of the football and softball teams; the extracurricular activities were extremely enjoyable and I will really miss playing with these teams. I also want to thank James Harris and Stephen Maldonado who both helped me with

my projects and were good friends. Furthermore, I am appreciative towards the remaining members of the Lewis group for all the advice and help. Also, I want to thank all the people I forgot to mention.

Lastly I want to thank my family, especially my wife Meagan who has provided incredible support and a welcome release from life at grad school. I am also extremely grateful for the new addition to our family, Ben.

ABSTRACT

ZnO nanowire arrays were synthesized by a simple wet chemical method, and the effects of substrate, solution composition, and time on the attributes of the wire arrays were explored. Optimized wire arrays were used as photoanodes for water oxidation and in dye-sensitized solar cells with fast redox couples. The results for the wire arrays as photoanodes for water oxidation were compared to single crystals. Both ZnO electrodes exhibited poor cathodic kinetics with the aqueous solution, resulting in a non-ideal behavior of the semiconductor-liquid junction and substantial losses in the fill factor. Surprisingly, the wire arrays approached the efficiency of the single crystal, 0.18% vs 0.22% respectively. In the dye sensitized solar cell, the ZnO nanowires developed a Schottky junction and allowed the use of fast redox couples. Unfortunately, the efficiencies measured were low, but results suggest the potential for substantial gains in the efficiency and versatility of the dye-sensitized solar cell.

TABLE OF CONTENTS

Acknowledgements.....	iii
Abstract.....	v
Table of Contents.....	vi
List of Schemes.....	viii
List of Figures.....	ix
List of Tables.....	xiii
Chapter 1: Introduction to Photoelectrochemical Cells	
1.1 Introduction.....	1
1.2 Photoelectrochemical Cells.....	3
1.2.1 Semiconductor Properties.....	3
1.2.2 Semiconductor – Liquid Junctions.....	8
1.2.3 Structured Electrodes.....	12
1.2.4 Types of Photoelectrochemical Cells.....	13
1.3 ZnO Nanowire Array PECs.....	15
1.4 References.....	16
Chapter 2: Exploration of the Wet Chemical Synthesis for ZnO Nanowire Arrays	
2.1 Introduction.....	17
2.2 Experimental.....	20
2.3 Results.....	21
2.3.1 Nanowire Growth on Different Substrates.....	21
2.3.2 Time Dependence.....	29
2.3.3 Concentration Dependence.....	34
2.3.4 Extending the Wire Growth.....	37
2.3.5 Peeled Wire Arrays.....	41

2.4 Discussion.....	43
2.5 References.....	46
Chapter 3: Comparison Between ZnO Nanowire Arrays and Single Crystals as Photoanodes for Water Oxidation	
3.1 Introduction.....	48
3.2 Background.....	50
3.3 Experimental.....	54
3.4 Results.....	57
3.4.1 Growth Conditions.....	57
3.4.2 Characterization.....	59
3.4.3 Water Oxidation Results.....	61
3.5 Discussion.....	72
3.5.1 Affect of the Anneal.....	72
3.5.2 Water Oxidation Kinetics.....	75
3.5.3 Difference Between the Single Crystal and Wire Arrays.....	78
3.6 References.....	81
Chapter 4: ZnO Nanowire Arrays in Dye-Sensitized Solar Cells with Fast Redox Couples	
4.1 Introduction.....	84
4.2 Experimental.....	87
4.3 Results.....	90
4.3.1 ZnO Nanowire Electrodes.....	90
4.3.2 Photoactive ZnO Nanowires in Aqueous $\text{Fe}(\text{CN})_6^{2+}$ / $\text{Fe}(\text{CN})_6^{3+}$	90
4.3.3 ZnO Nanowire DSSC with Fast Redox Couple.....	93
4.3.4 ZnO Nanowire Arrays with CdS Quantum Dots.....	97
4.4 Discussion.....	99
4.5 References.....	102

LIST OF SCHEMES

Scheme 1.1: Band Bending.....	10
Scheme 1.2: Planar vs Wire Array	14
Scheme 3.1: Band Bending.....	51
Scheme 4.1: Rates at the working electrode in a typical DSSC.....	86

LIST OF FIGURES

Figure 1.1: Solar Irradiance for AM 1.5.....	4
Figure 2.1: Wurtzite crystal structure.....	18
Figure 2.2: Nanowire growth from a 25 mM solution with ZnO nanoparticles as the seed layer on FTO. Zoomed out image (a) shows two different growth regions: nanowire growth (b) and branching growth (c). For a few substrates, the branching region covered the majority of the area (d).....	22
Figure 2.3: Nanowires on piranha cleaned FTO grown from a 25 mM solution.....	24
Figure 2.4: Nanowires on plasma ashed FTO grown from a 50 mM solution.....	25
Figure 2.5: Nanowires on a thin film of ZnO on FTO grown from a 50 mM solution.....	27
Figure 2.6: Nanowires on Zn foil grown from a 50 mM solution.....	28
Figure 2.7: Time dependant study of nanowires on plasma cleaned FTO grown from a 50 mM solution. Side views of wires grown for 2 hrs (a), 4 hrs (b), 6 hrs (c), and 12 hrs (d). Top view of wires grown for 12 hrs (e) and 18 hrs (f).....	31
Figure 2.8: Time dependant study of nanowires on a thin film of ZnO on FTO grown from a 50 mM solution. Side view of wires grown for 2 hrs (a) and 4 hrs (b). Top view of wires grown for 2 hrs (c) and 4 hrs (d).....	32
Figure 2.9: Irregular time dependant growth for nanowires on Zn Foil grown from a 50 mM solution. Top view for growth times of 2 hrs (a), 4 hrs (b), 6 hrs (c), 14 hrs (d) 18 hrs (e), and 18 hrs at a lower magnification (f).....	33
Figure 2.10: Concentration dependence for nanowires of a thin film of ZnO on FTO. Top view of 5 mM (a), 25 mM (b), 50 mM (c), and 75 mM (d) solution concentrations.....	35

Figure 2.11: Concentration dependence for nanowires of a thin film of ZnO on FTO. Side view at 70° of 5 mM (a), 25 mM (b), 50 mM (c), and 75 mM (d) solution concentrations.....	36
Figure 2.12: Extended growth for nanowires on a thin film of ZnO on FTO. The wires were grown from a 50 mM solution and the solution was replaced after 4 hrs and the growth was extended for an additional 4 hrs. Top view (a) and side view (b).....	38
Figure 2.13: Nanowires on thin film of ZnO on FTO grown for 110 hrs in a continuous flow of a 5 mM solution with the solution replaced every 3 hrs. Top view (a) and side view (b)....	39
Figure 2.14: Nanowires on thin film of ZnO on FTO grown for 36 hrs in a continuous flow of a 50 mM solution with the solution replaced every 3 hrs.	40
Figure 2.15: Short (a) and long (b) nanowire arrays encased in PDMS	42
Figure 3.1: SEM images of the side and top view of ZnO nanorods grown from a: 5 mM solution for 4 hrs (a, b), 50 mM solution for 4hrs (c, d), and a 50 mM solution for 4 hrs followed by 4 hrs in a fresh 50 mM solution (e,f).....	58
Figure 3.2: XRD of the ZnO nanowire films as grown and after annealing at 450 °C for two hours in air. The asterisk indicates peaks from the FTO.....	60
Figure 3.3: Absorbance spectra of the 5 mM ZnO nanowires.....	60
Figure 3.4: AM1.5 response of ZnO single crystals in 0.5 M K ₂ SO ₄ at pH 6.4. Black curve was etched in H ₂ SO ₄ where the red curve was etched in H ₃ PO ₄	62
Figure 3.5: Photoresponse of the as grown nanorods (blue), annealed nanorods (black) and the 20 nm ZnO seed layer (red) to 365 nm light.....	64
Figure 3.6: 365 nm photoresponse of 2 μm (blue) and 4 μm (black) length wire arrays in 0.5 M K ₂ SO ₄ at pH 6.4.....	64
Figure 3.7: AM 1.5 light and dark curves of the single crystal (black) and 4 μm length wire arrays (blue) in 0.5 M K ₂ SO ₄ at pH 6.4.....	66

- Figure 3.8:** AM 1.5 with 385 nm long pass filter photoresponse of single crystal (black) and 4 μm length wire arrays (blue) in 0.5 M K_2SO_4 at pH 6.4..... 66
- Figure 3.9:** AM 1.5 light and dark curves of ZnO single crystal (black) and 4 μm length wires (blue) in 0.5M K_2SO_4 pH 11 with O_2 bubbling..... 68
- Figure 3.10:** AM 1.5 with 385 nm long pass filter photoresponse of single crystal (black) and 4 μm length wires (blue) to in 0.5M K_2SO_4 pH 11 with O_2 bubbling 68
- Figure 3.11:** Spectral Response of the 4 μm wires (blue) and the single crystal (black) in 0.5M K_2SO_4 pH 11 no bubbling.....71
- Figure 3.12:** Detailed XPS scans of the carbon (a) and nitrogen (b) regions for the as grown and annealed wire arrays 73
- Figure 3.13:** Photoresponse to 365 nm light for the 4 μm length nanowire arrays (a) and the single crystal (b). The power intensities were 3.02, 2.52, 1.26, 0.862, 0.37 mW/cm^2 76
- Figure 3.14:** Plot of light intensity versus J_{sc} for the 4 μm length nanowire arrays (\bullet) and the single crystal (+)..... 77
- Figure 4.1:** ZnO nanowire arrays grown the hydrothermal method. (a) is the short array and (b) is the long array.....91
- Figure 4.2:** Am 1.5 light and dark responses of bare 4 μm long ZnO nanowire arrays in a 10 mM $\text{Fe}(\text{CN})_6^{2-}$ / 1 mM $\text{Fe}(\text{CN})_6^{3-}$ aqueous solution with 0.5 M K_2SO_4 92
- Figure 4.3:** AM 1.5 with 385 nm long pass filter light and dark response of long nanowire arrays sensitized with N719 dye in 1 mM Fc / 0.1 mM Fc^+ solution with 0.1 M LiClO_4 (black). Dark curve for the ZnO single crystal in the same solution (blue)..... 94
- Figure 4.4:** AM 1.5 with 385 nm long pass filter light and dark responses of the long wires with N719 dye in 1mM BrFc / 0.1mM BrFc^+ in acetonitrile with 0.1 M LiClO_4 . The three light curves show the decrease in efficiency for each subsequent scan..... 96
- Figure 4.5:** AM 1.5, with 385 nm long pass filter, light and dark response of short nanowire array sensitized with CdS quantum dots in a 0.1 M Na_2S / 0.1 M S aqueous 1 M KOH electrolyte. 98

Figure 4.6: E-beam patterned Ti / Au contacts on a single ZnO nanowire (a). 4-point resistance measurements of the nanowire (b)..... 101

LIST OF TABLES

Table 3.1: AM 1.5 response for ZnO single crystal and 4 μm length nanowire arrays in 0.5 M K_2SO_4 at pH 11 with O_2 bubbling.....	69
Table 3.2: AM 1.5 with 385 nm long pass filter response for ZnO single crystal and 4 μm length nanowire arrays in 0.5 M K_2SO_4 at pH 11 with O_2 bubbling.....	69

Chapter 1

Introduction to Photoelectrochemical Cells

1.1 Introduction

World energy demand is currently ~ 0.5 ZJ ($1 \text{ ZJ} = 1 \times 10^{21} \text{ J}$) with a mean consumption rate of 15 TW.¹ Energy use has risen on average by $\sim 2.4\%$ per year for the past 25 years and projections are that world energy use will increase $\sim 50\%$ by 2030.¹ The world now obtains $>80\%$ of its energy from fossil fuels. With the prospect of significant climate change and other environmental impacts due to the build up of CO_2 in the atmosphere, the need for a significant source of carbon neutral energy has become apparent. Currently, few renewable energy options contribute significantly to our energy needs; however, the sun provides 1.2×10^5 TW of power to the earth, and in one hour more than 0.4 ZJ of solar energy strikes the earth.² Thus, in a little more than one hour, enough solar energy falls on the earth to provide the yearly energy needs of the planet. We would only need to convert 0.01% of the incoming solar radiation to supply the world's energy needs, using, for example, single crystal photovoltaic (PV) technology, which can have solar conversion efficiencies as high as 40%.³

Thus, one may wonder what is the energy crisis and why are we still using fossil fuels? The answer, of course, lies in the economics of solar conversion. Currently, the cost of electricity from high efficiency PVs is ~ 5 times more

expensive than electricity from fossil fuels, and PV energy is even more expensive than fossil fuels, on an energy basis. In fact PVs produce energy that costs ~ 20 -50 times that produced from fossil fuels.² One problem with photovoltaic devices is the high cost of materials in the solar cell. If one considers silicon, the raw materials are inexpensive, since Si is the eighth-most common element. Unfortunately, the solar light absorptivity of silicon is low, and thus, a thick piece (~ 100 mm) of silicon is needed to absorb most of the incoming solar radiation. For planar solar cells, this means that the electron/hole pair produced by the absorption of a solar photon must survive long enough for the electron or hole to transverse the thick slab of Si and reach the semiconductor junction where charge collection can be achieved. Thus, the silicon used in solar cells must be very high purity and well passivated, so that the rate of electron-hole recombination is slow and the excitation is not lost. For single-crystal PV, high-purity materials are needed to obtain high efficiencies, resulting in expensive processing techniques.

The other problem with PVs is regarding the type of energy produced. PVs convert sunlight directly into electricity that must be used or stored immediately and when the sun sets the solar cells stop producing electricity. In order to provide uninterrupted power generation, an energy storage device must be an active part of the PV system. Plants have already solved the problem of the lack of sunlight at night by using solar energy to drive chemical reactions. For photosynthesis, the solar energy is stored in chemical bonds that can be transported and stored to provide uninterrupted energy at remote locations.

With the high costs associated with PV, it is clear why solar energy does not significantly contribute to the world energy production. Different solar conversion strategies are needed to reduce the cost. Photoelectrochemical cells (PECs) are an attractive alternative to PV because of the ability to directly produce electricity or chemical fuels. PECs consist of a semiconductor-liquid junction and have the same semiconductor requirements as PVs. Fortunately, the use of structured electrodes, such as wire arrays, is theorized to produce high solar conversion efficiencies for low quality semiconductor materials.⁴ Using both PECs and structured electrodes, significant reductions in solar energy can theoretically be achieved. The focus of my thesis is to explore the use of the inexpensive structured semiconductor materials for use in PECs.

1.2 Photoelectrochemical Cells

1.2.1 Semiconductor Properties

PECs consist of a semiconductor-liquid junction and usually separate and collect photogenerated charges similar to PVs. In these types of PECs, the semiconductor properties determine the solar energy conversion potential; therefore, they must be fully understood to extract the maximum efficiency. One of the main properties of a semiconductor is the band gap between the valence and conduction bands. Like other solids, electrons reside in energy bands that arise from the mixing of atomic orbitals. In all solids, the atomic orbitals of the material mix and create energy bands. In a semiconductor, the valence band is essentially full, while the conduction band is essentially empty. The gap between the valence

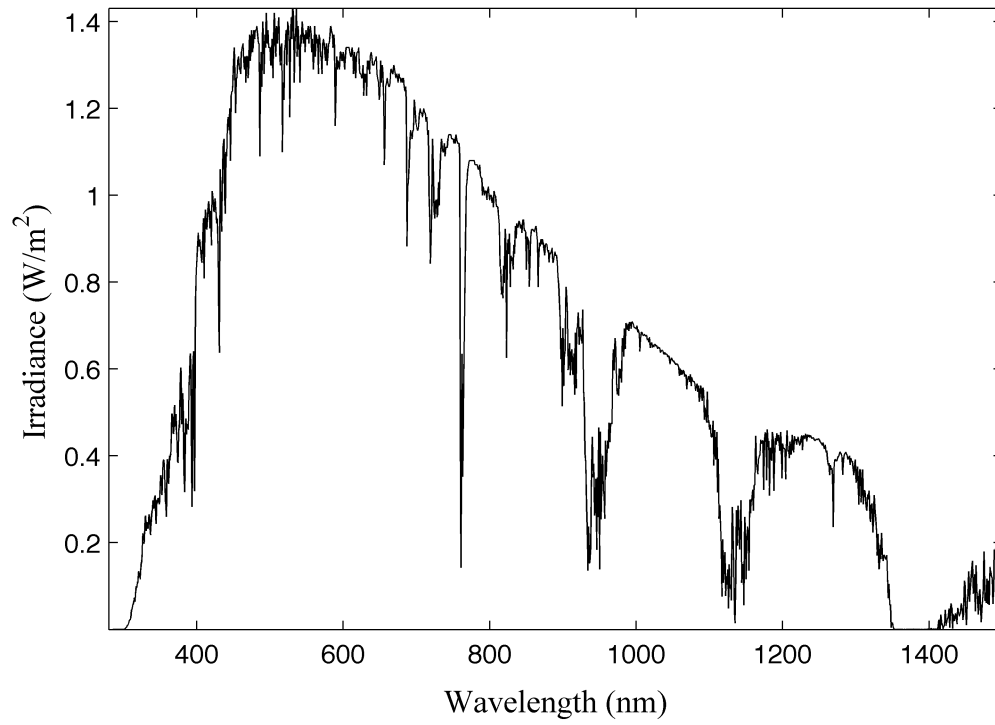


Figure 1.1: Solar Irradiance for AM 1.5.

and conduction bands determines the absorption properties of the material and the maximum solar energy conversion for the semiconductor.

Electrons are promoted from the valence band to the conduction band by the absorption of light. The band gap sets the minimum energy required to promote electrons and any excess energy adsorbed is quickly lost to heat as the excited electron quickly relaxes to the lowest energy level in the conduction band. The solar spectrum can be seen in Figure 1.1. Semiconductors with small band gaps generate more current because of the abundance of photons with energy greater than the band gap. Unfortunately, the potential difference is small and the voltage generated will be small. Likewise, semiconductors with large band gaps will have large voltages, but small currents. The ideal band gap, based on the solar spectrum, is around 1.0 eV to 1.7 eV with a maximum efficiency of 30%.

The band gap also determines the material thickness. There are two types of transitions that occur between the valence band and conduction band: indirect and direct. With a direct transition, the promotion of an electron occurs by the adsorption of a photon, where an indirect transition requires both a photon and phonon. The indirect transitions have small absorption coefficients and for materials like silicon, 100 μm or more are required to absorb the majority of the incident light. Direct band gaps have significantly higher absorption coefficients and require a thickness of only a few microns. Direct band gaps have the advantage of requiring less material, but in terms of conversion efficiency the two are basically the same. In the direct band gap semiconductor, the photogenerated carriers may

have a diffusion distance, but the recombination rates are higher due to the favorable transition.

While the band gap determines the photo properties, the equilibrium carrier concentrations determine the conductivity and electrical behavior of the semiconductor. At 0 K all the states in the valence band are full and all the states in the conduction band are empty. As the temperature increases, electrons are promoted to the conduction band and holes are created in the valence band by thermal excitation. Using the Boltzmann relationship, the equilibrium carrier concentration can be determined by equation 1.1:

$$np = n_i^2 = N_c N_v \exp\left(-\frac{E_g}{kT}\right) \quad (1.1)$$

where n and p are the electron and hole concentrations respectively, N_c and N_v are the effective density of states in the conduction and valence band respectively, E_g is the band gap, k is Boltzmann's constant and T is the temperature. With thermal excitation, each excited electron creates a hole and therefore $n = p$ and the equilibrium carrier concentration is n_i^2 .

In semiconductors, n_i^2 is so low that even part per billion levels of impurities significantly alter the electrical properties. By adding specific dopants, the electrical properties can be tailored to improve the solar energy conversion efficiency. There are two different types of dopants, donors and acceptors. Dopants with populated energy levels near the conduction band are donors because the atom is readily ionized and donates a free electron to the conduction band. Likewise,

semiconductors doped with acceptors have vacant energy levels near the valence band and the atom ionizes the semiconductor to create excess holes.

Semiconductors doped with donors are called n-type because of the excess electrons while semiconductors doped with acceptors are called p-type. In the case of Si, which is a Group 14 element, n-type dopants would be Group 15 elements like P or As. For the Group 15 elements, only four of the five valence electrons participate in tetrahedral bonding. At room temperature, the fifth valence electron is donated to the conduction band. Likewise, Group 13 elements like B and Al have only three valence electrons and will ionize a silicon atom for tetrahedral bonding, creating excess holes and p-type doping. Both dopants and impurities change the equilibrium carrier concentrations, but the relationship in equation 1.1 is still valid. Even though equation 1.1 was derived for an intrinsic semiconductor, the equilibrium constant relationship of the right side will hold for dopants and impurities.

The large changes in the electron and hole concentration due to dopants and impurities causes significant shifts in the electrochemical potential, or Fermi level, E_F , of the semiconductor. As defined by statistical mechanics, the Fermi level is the energy level where the probability of finding an electron is $\frac{1}{2}$. For an intrinsic semiconductor at 0K this level would be in the middle of the band gap. The probability of finding the electron would be 1.0 in the valence band and 0 in the conduction band; therefore, the Fermi function will have a value of $\frac{1}{2}$ in the middle of the band gap. As the temperature increases, thermally excited electrons are promoted to the conduction band, leaving the same number of holes in the

conduction band. E_F will remain essentially in the middle of the band gap with only slight deviations due to any difference between the density of states in the conduction band and valence band. Introducing dopants or impurities creates excess carriers, shifting E_F from the intrinsic level. For electron donors, E_F will shift towards the conduction band, while acceptors shift E_F towards the valence band, equations 1.2 and 1.3:

$$E_F = E_{cb} - kT \ln\left(\frac{n}{N_c}\right) \quad (1.2)$$

$$E_F = E_{vb} - kT \ln\left(\frac{p}{N_v}\right) \quad (1.3)$$

where E_{cb} and E_{vb} are energy potentials of the conduction band and valence band respectively, k is Boltzmann's constant, and T is the temperature.

For ZnO, with a 3.3eV band gap, the number of thermally excited electrons is so small that impurities dominate the electronic properties. In ZnO, the electrically active impurities are usually due to either O vacancies or reduced Zn and result in an n-type behavior.⁵ Intentional doping can tailor the electronic properties to produce even p-type behavior, but the dopant concentration must be greater than the impurity concentration.⁶⁻⁸

1.2.2 Semiconductor - Liquid Junctions

When a semiconductor is in contact with a redox active solution, an electric field is present at the interface. This electric field arises from the potential difference between E_F and the electrochemical potential of the solution. Scheme 1.1a is the energy diagram of an n-type semiconductor and a redox active solution

prior to contact. With E_F of semiconductor higher than the solution potential, electrons will flow from the semiconductor into the solution upon contact. This will deplete the electrons at the surface of the semiconductor, resulting in a build-up of positive charge, while a negative charge builds up at the surface in the solution. Electrons flow until the electric field at the interface offsets the difference between E_F and the solution potential. With the electric field, electrons near the surface will have a higher potential than ones in the bulk of the semiconductor, resulting in a bending of the energy bands near the surface that is directly proportional to the field strength, Scheme 1.1b. The extent of band bending is determined by equation 1.4:

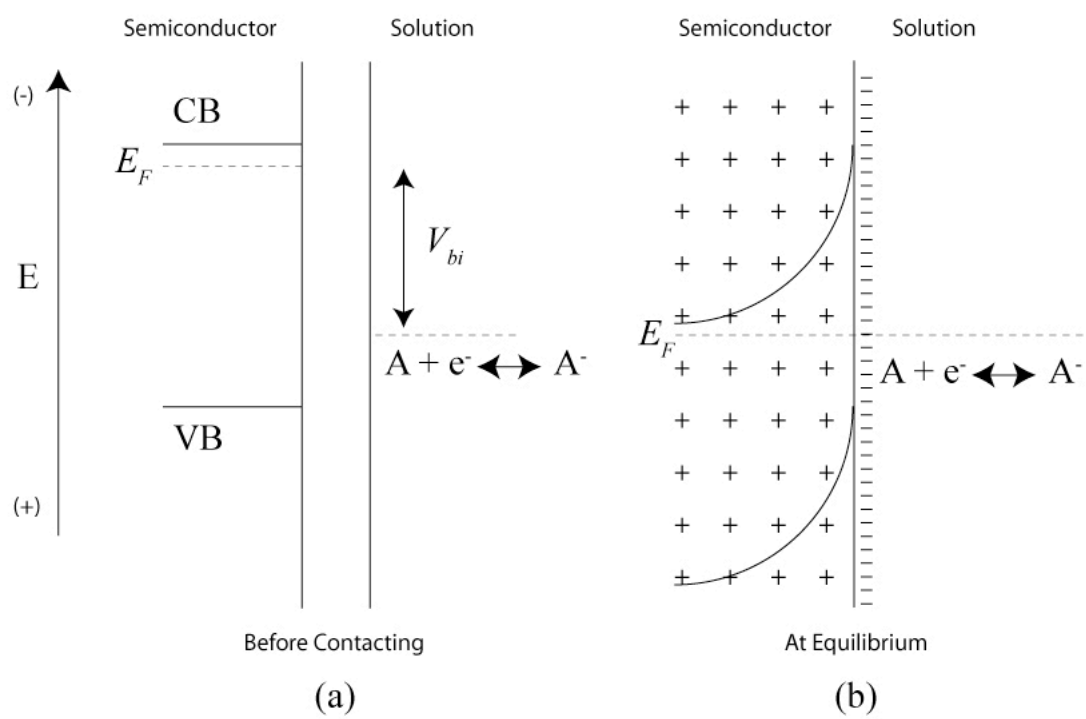
$$w = \sqrt{\frac{2\epsilon_s V_{bi}}{qN_d}} \quad (1.4)$$

where w is the depletion width and represents how far the electric field extends into the semiconductor, V_{bi} is the built-in voltage and is determined by the potential difference between E_F and the solution potential, N_d is the dopant density, and ϵ_s is the dielectric constant of the semiconductor.

For n-type semiconductors in the dark, the current is carried by electrons, the majority carriers, and follows the diode equation, equation 1.5:

$$I = I_o \left[\exp\left(\frac{-qV}{kT}\right) - 1 \right] \quad (1.5)$$

where I is the current, I_o is the exchange current and V is the applied voltage. The value I_o is determined by the equilibrium kinetics of the semiconductor-liquid junction. While no net current can be generated at equilibrium, there is an equal



Scheme 1.1: Band Bending.

flux of electrons, I_o , in both directions at the interface. I_o is dependant on the surface electron concentration at equilibrium, n_{so} , the rate constant for electron transfer, and the solution composition. From equation 1.5, at negative voltages, current is exponentially dependant on voltage, but for positive voltages the current is essentially independent. This behavior is known as rectification and describes the passage of current predominately in one direction.

Under illumination, the absorption of light generates electron hole pairs at a rate proportional to the photon flux, Γ . For normal solar applications, the number of electrons generated is insignificant to the concentration of dopants and does not alter the majority carrier current. In contrast, the equilibrium concentration of holes is small and the photogenerated holes significantly alter the minority carrier current. Photogenerated holes diffuse to the interface and oxidize donors in the solution. The rate of this reaction is proportional to $\Phi\Gamma$, where Φ is the charge collection efficiency, and the current generated, I_{ph} , exists as an offset to the current obtained in the dark, equation 1.6:

$$I = I_{ph} - I_o \left[\exp\left(\frac{-qV}{kT}\right) - 1 \right] \quad (1.6)$$

The solar energy conversion performance of a photoelectrochemical cell is determined from the short circuit density, J_{sc} , the open circuit voltage, V_{oc} , and the fill factor, ff, equation 1.7:

$$Eff\% = \frac{J_{sc} V_{oc} ff}{P_{in}} \times 100\% \quad (1.7)$$

Equation 1.7 is merely the power out, determined from the current – voltage curve, divided by the power in, P_{in} , from the illumination intensity. J_{sc} is the current density at 0 applied potential. V_{oc} is the potential at 0 current and is determined by equation 1.8:

$$V_{oc} = \frac{kT}{q} \ln\left(\frac{I_{ph}}{I_o}\right) \quad (1.8)$$

Equation 1.8 is obtained by setting equation 1.6 equal to 0. The fill factor represents how well the current - voltage curve under illumination, fills out the rectangle defined by J_{sc} and V_{oc} , and the fill factor is the ratio of the max power on the curve and the product of J_{sc} and V_{oc} .

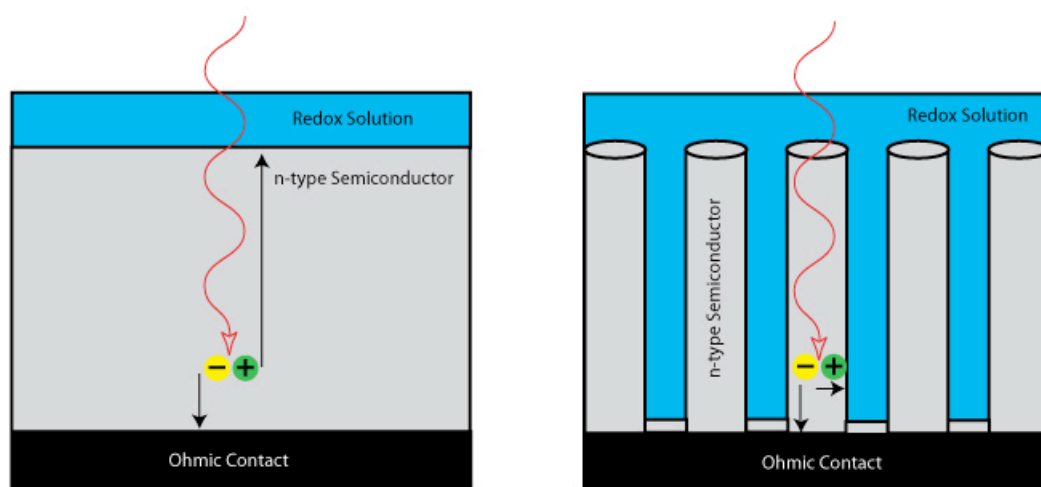
1.2.3 Structured Electrodes

Structured electrodes, such as wire arrays, are theorized to improve the efficiency of lower quality semiconductors and reduce the cost of solar energy conversion.⁴ The improvement in efficiency is due to higher charge collection efficiencies for low minority carrier diffusion length materials. In a planar electrode, electron hole pairs are generated throughout the material and the minority carrier must diffuse to the interface, Scheme 1.2a. For high collection efficiencies, the minority carrier diffusion length must be at least the same as the absorption length. Only high purity samples have long diffusion lengths because any lattice defects or impurities are frequently active recombination sites and reduce the lifetime of the photogenerated carriers.

Unlike the planar design, high charge collection efficiencies are possible in low diffusion length materials.^{4,9} All the photogenerated minority carriers in an individual wire have the same diffusion length equal to the radius of the wire, Scheme 1.2b. In the optimal wire array, the length of the wire is matched to the absorption length and the radius is matched to the minority carrier diffusion length. Unlike the planar electrode, the optimal wire array will have a high collection efficiency even for semiconductors with minority carrier diffusion length shorter than the absorption length.

1.2.4 Types of Photoelectrochemical Cells

There are two different types of PECs: regenerative and photosynthetic. The regenerative cells operate in a similar manner to PVs and produce only electricity. For an n-type semiconductor, holes oxidize donors at the surface of the semiconductor, while at the counter electrode, the oxidized donors are reduced back to their original form. The regenerative cells have no net change in the composition of cell. The energy produced by the cell is used to supply electricity to external devices. The energy produced in a photosynthetic cell is stored in chemical bonds and results in a change in the solution composition. One compound is oxidized at the surface of an n-type semiconductor while a completely different compound is reduced at the counter electrode. An example of a photosynthetic cell is the photoelectrochemical splitting of water to H_2 and O_2 . The oxidation of water to O_2 occurs at one electrode while the reduction of protons to H_2 occurs at the other.



(a)

(b)

Scheme 1.2: Planar vs Wire Array.

1.3 ZnO Nanowire Array PECs

The goal of my thesis is to explore the use of ZnO nanowire arrays in photoelectrochemical cells. I chose ZnO because of the simple wet chemical synthesis for highly crystalline nanowire arrays on various substrates.¹⁰ With the large band gap, 3.3 eV, ZnO absorbs a small portion of the solar spectrum. Photoelectrochemical cells with ZnO as the photoactive materials, will have severe limits on efficiency, but the wire arrays provide useful information on the benefits and drawbacks of using structured electrodes. In the following chapters, I will explore the affect of the growth parameters on the attributes and properties of the wires as well as the use of the ZnO nanowire arrays in regenerative and photosynthetic PECs.

1.4 References

- (1) International Energy Outlook 2007, Energy Information Administration, **2007**, Report number DOE/EIA-0484(2007).
- (2) Lewis, N. S.; Nocera, D. G. *P Natl Acad Sci USA* **2006**, *103*, 15729.
- (3) King, R. R.; Law, D. C.; Edmondson, K. M.; Fetzer, C. M.; Kinsey, G. S.; Yoon, H.; Sherif, R. A.; Karam, N. H. *Appl Phys Lett* **2007**, *90*, 183516.
- (4) Kayes, B. M.; Atwater, H. A.; Lewis, N. S. *J. Appl. Phys.* **2005**, *97*.
- (5) Kohan, A. F.; Ceder, G.; Morgan, D.; Van de Walle, C. G. *Phys. Rev. B* **2000**, *61*, 15019.
- (6) Look, D. C.; Reynolds, D. C.; Litton, C. W.; Jones, R. L.; Eason, D. B.; Cantwell, G. *Appl. Phys. Lett.* **2002**, *81*, 1830.
- (7) Tsukazaki, A.; Ohtomo, A.; Onuma, T.; Ohtani, M.; Makino, T.; Sumiya, M.; Ohtani, K.; Chichibu, S. F.; Fuke, S.; Segawa, Y.; Ohno, H.; Koinuma, H.; Kawasaki, M. *Nature Materials* **2005**, *4*, 42.
- (8) Ozgur, U.; Alivov, Y. I.; Liu, C.; Teke, A.; Reshchikov, M. A.; Dogan, S.; Avrutin, V.; Cho, S. J.; Morkoc, H. *J. Appl. Phys.* **2005**, *98*.
- (9) Maiolo, J. R.; Atwater, H. A.; Lewis, N. S. *J. Phys. Chem. C* **2008**, *112*, 6194.
- (10) Vayssieres, L.; Keis, K.; Lindquist, S. E.; Hagfeldt, A. *J. Phys. Chem. B* **2001**, *105*, 3350.

Chapter 2

Exploration of the Wet Chemical Synthesis for ZnO

Nanowire Arrays

2.1 Introduction

ZnO is a popular wide band gap semiconductor with applications in photovoltaics, electronics, optics, sensing, and catalysis.^{1,2} Recent research efforts have focused on ZnO nanostructures, such as nanowire arrays, and their unique properties.³⁻⁵ High quality ZnO nanowire arrays can be grown by either chemical vapor deposition (CVD) or by a wet chemical synthesis.^{6,7} For CVD, growth occurs by a vapor-liquid-solid (VLS) mechanism at temperatures around 700°C with Au as the catalyst. In contrast, the wet chemical method proceeds by hydrothermal synthesis at temperatures below 100°C and without the need for an expensive catalyst. With both methods producing high quality single crystal wire arrays on various substrates, the simplicity of the wet chemical synthesis makes it an obvious choice.

The basic procedure for nanowire array growth is to place the substrate in a hexamine (hex) / zinc nitrate aqueous solution and heat to 80-95 °C. At the elevated temperature, epitaxial growth occurs by the proposed reactions 2.1-2.3, where hex

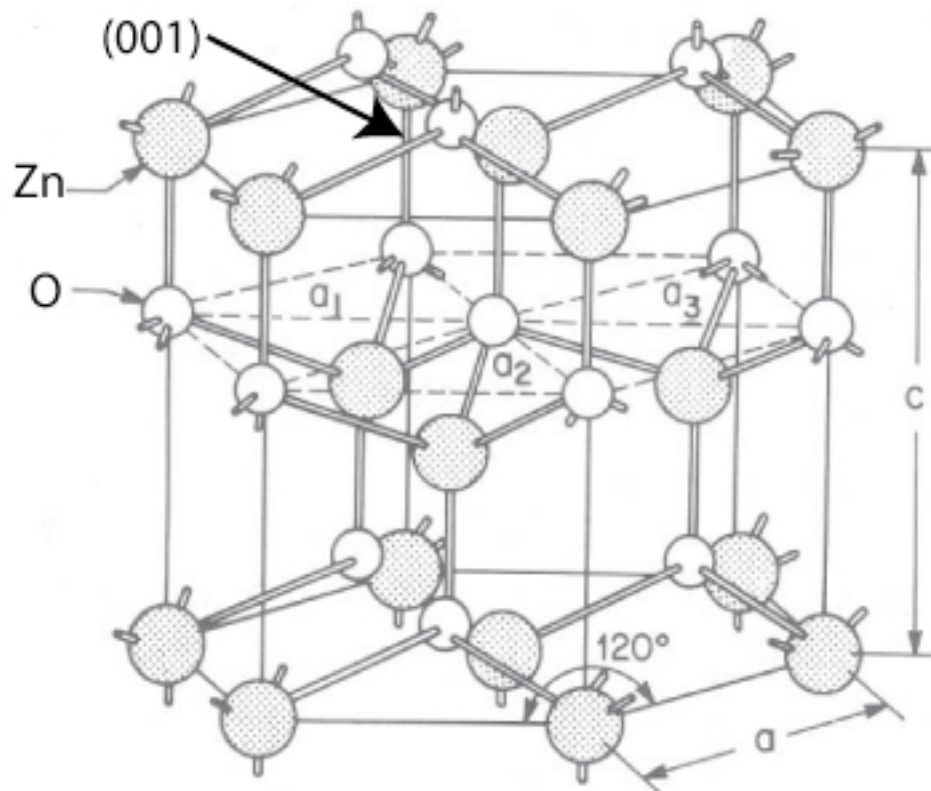


Figure 2.1: Wurtzite crystal structure.

decomposes slowly and increases the pH. At the higher pH, ZnO begins to precipitate and seeded growth occurs perpendicular to the substrate.



For nanowire growth, hex and zinc nitrate are always in a 1:1 ratio. The wire attributes can be customized simply by varying the concentrations of the two compounds, still in the 1:1 ratio, and the time of the growth.⁸

Wurtzite is the thermodynamically stable crystal structure at ambient conditions for ZnO. The wurtzite structure has a hexagonal unit cell with two lattice parameters, *a* and *c*, Figure 2.1. Nanowire growth occurs along the *c*-axis where the polar (001) face is 'metastable' and has the highest crystal growth velocity.^{7,9} The (001) face differs from the other crystal faces by its polar nature and composition of either all zinc atoms or all oxygen atoms. Furthermore, there is no center of inversion and asymmetry along the *c*-axis allows for anisotropic growth.

While the wet chemical method has been around and widely used since 2001, there are still questions dealing with the growth time and substrate. One major issue deals with seeding the growth on the substrate. There are reports of heteronucleation occurring directly on FTO producing high-density wire arrays^{7,8}, but the majority of the literature procedures use a ZnO seed layer.¹⁰⁻¹² The most common seed layer is a ZnO nanoparticle film. Growth times and temperatures also vary widely between the different procedures and produce disparate results. At long growth times, there have even been reports of nanotube growth.^{11,13-15} In this

chapter the effect of the substrate, reaction time, and concentration on the wire attributes is explored.

2.2 Experimental

Four different substrates were used: fluorine doped tin oxide on glass (FTO) TEC 25 purchased from Hartford Glass, Zn foil 99.9% purchased from Aldrich, FTO with ZnO nanocrystalline particle coating and FTO with a thin film of ZnO. The chemicals, hexamine 98% and zinc nitrate hexahydrate 98% were purchased from Aldrich and used as received.

ZnO nanoparticles were synthesized by a literature procedure.¹⁶ Briefly, 125 mL of 0.01 M zinc acetate in methanol was heated to 60 °C. KOH, 0.03 M in methanol, was slowly added to the Zn²⁺ solution over the course of 1 hr. Then the solution was heated for an additional 2 hr at 60 °C. After cooling, the solution was rotovaped to 100 mL. FTO slides were dipped in the nanoparticle solution and allowed to air dry before heating to 140 °C for 30 min. The ZnO thin film was grown by sputtering ~20 nm of Zn on FTO and then thermally oxidizing in air at 400°C for 2 hrs.

For nanowire growth, the substrate was placed in an aqueous solution with equal concentrations of zinc nitrate and hex. Two different reaction vessels were used, either a round bottom flask and reflux condenser in an oil bath or a capped pyrex bottle in an oven. With the round bottom flask, the substrate was suspended in the stirred solution, while with the bottle, the substrate was merely placed in the unstirred solution. After heating to 95°C for the specified time, the solution was

briefly allowed to cool before removing the substrate and thoroughly rinsing with water. For extended growth, a peristaltic pump was used to replace the solution every 3 hours.

Scanning Electron Microscopy was used to characterize the physical attributes of the arrays. The SEM was a Zeiss 1550 VP Field Emission SEM in the geology department at Caltech. Average lengths and diameters were calculated from a representative image of the electrode.

2.3 Results

2.3.1 Nanowire Growth on Different Substrates

Initial attempts at wire growth used a round bottom flask with ZnO nanoparticles as a seed layer. The appropriate amounts of zinc nitrate and hex were weighed out and water was added to make a 25 mM solution. The resulting solution had a suspended white precipitate and was slightly opaque. After 2 hrs at 95 °C, there was a white precipitate on both sides of the FTO slide and on the flask that did not rinse off. Also, the growth solution was completely opaque due to white precipitates.

SEM images, Figure 2.2, showed that nanowire growth occurred on the substrate. In the zoomed out image, Figure 2.2a, the majority of the substrate has nanowire growth, but there are regions of extreme branching. Zooming in on the nanowires, Figure 2.2b shows that the diameter of the wires is less than 100 nm and there is small size dispersion. For some wires, the hexagonal shape is evident from the facets of the different crystal faces. Furthermore, there is a high density of wires

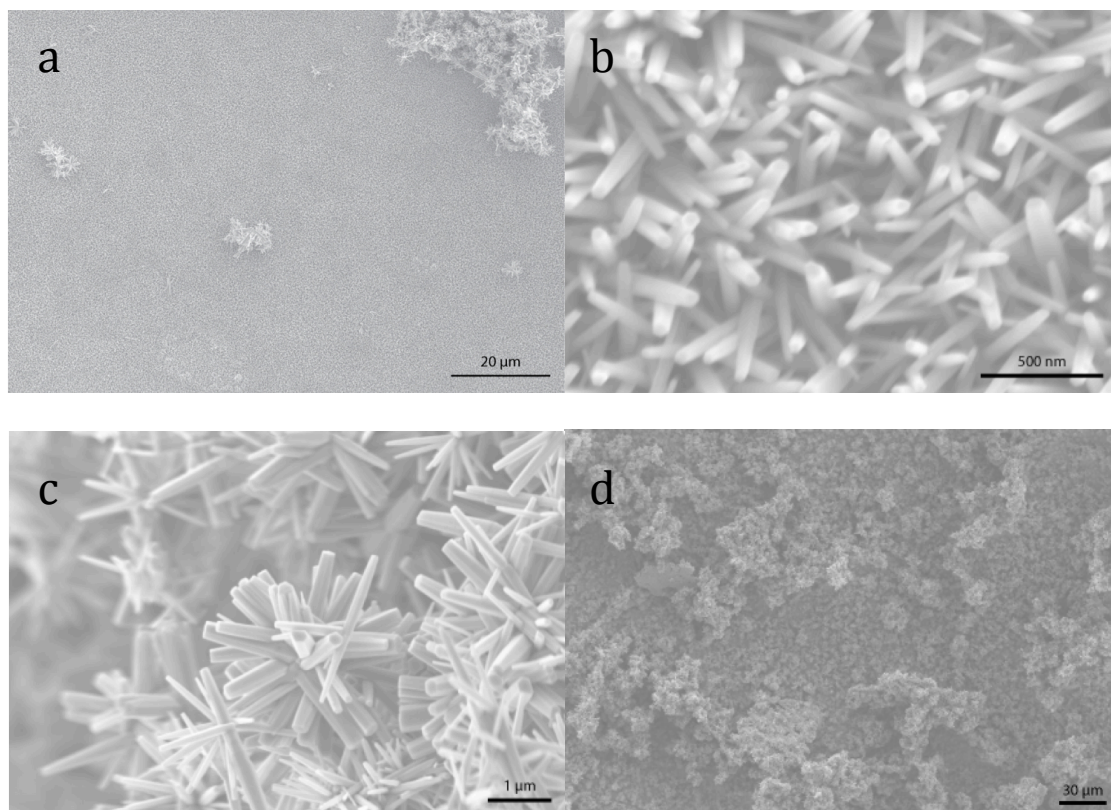


Figure 2.2: Nanowire growth from a 25 mM solution with ZnO nanoparticles as the seed layer on FTO. Zoomed out image (a) shows two different growth regions: nanowire growth (b) and branching growth (c). For a few substrates, the branching region covered the majority of the area (d).

and the growth is mainly perpendicular to the substrate. In Figure 2.2c, zooming in on the branching region, the growth appears more rapid and uncontrolled in these regions. Numerous wires extended in all directions from one central area, and the structure extends far above the substrate. On some substrates, using the same growth procedure, the branching region dominated the slide, Figure 2.2d. Even switching to the capped bottle reaction flask produced the same branching areas. In the literature, there are examples of flower-like structures that are similar to the branching region.¹⁷⁻¹⁹ Typically, the aqueous solution growth for the flower-like structures occurs at high ratios of OH^- to Zn^{2+} . While the branching areas are interesting, the focus is on the nanowire film and requires a more homogenous and reproducible array.

After talking with Dr. Lionel Vayssieres about ZnO nanowire growth, the setup was modified based on his recommendations. The substrate was switched to bare FTO cleaned in a piranha solution. The slide was placed diagonally, with the FTO side face down, in a capped bottle to be heated in an oven. One other modification was made in the solution preparation. The hex was dissolved in water prior to the addition of the zinc nitrate in order to prevent the precipitation of ZnO before heating. The resulting growth solutions were more transparent; however, at the higher concentrations like 50 mM and 75 mM there was still a suspended white precipitate.

After 3 hours of growth in a 25 mM solution, using the modifications suggested by Dr. Vayssieres, the FTO had a thin film on both sides. Upon rinsing

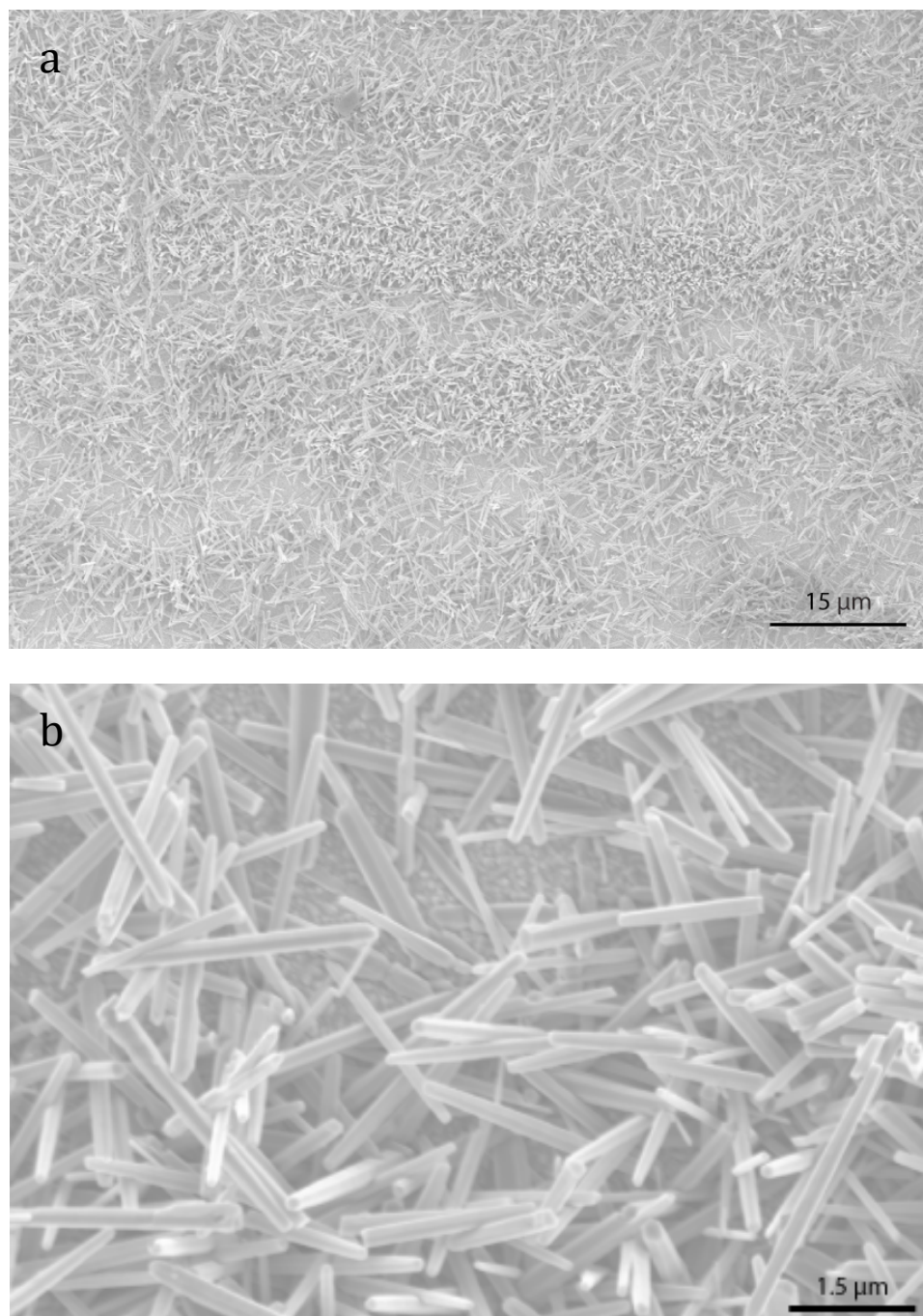


Figure 2.3: Nanowires on piranha cleaned FTO grown from a 25 mM solution.

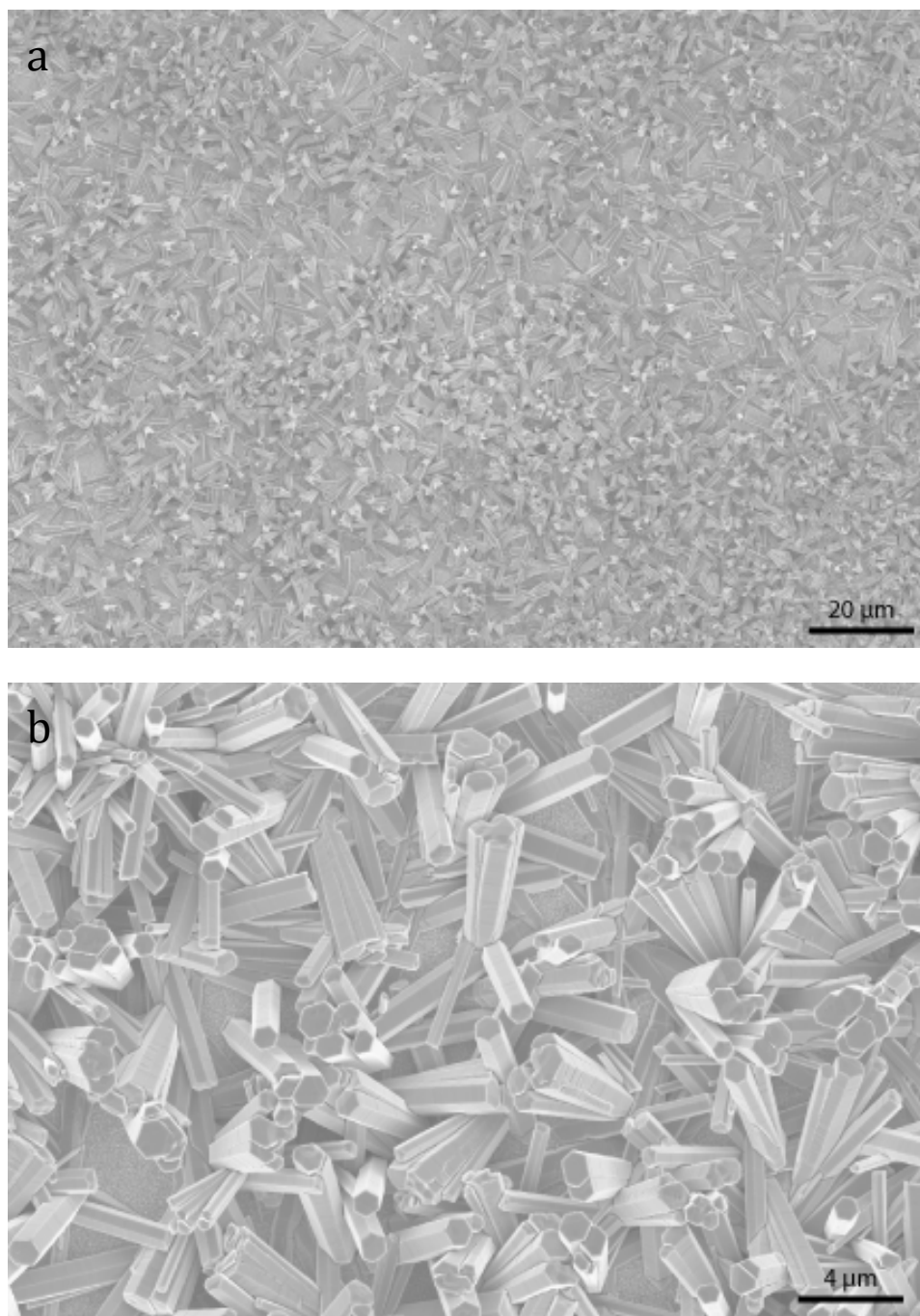


Figure 2.4: Nanowires on plasma ashed FTO grown from a 50 mM solution.

with water, the white film on the backside rinsed off, while the FTO side film did not. SEM images of the thin film on the FTO are shown in Figure 2.3. The growth on the film was almost entirely nanowires. Unfortunately, the wire density varied widely with a substantial area of bare FTO. In an attempt to better clean the surface and increase the wire density, the FTO was cleaned in a plasma asher. Figure 2.4 shows the SEM images of the plasma ashed substrates in a 50 mM solution. The wire density is worse than the piranha cleaned FTO and quite a few of the wires grew from one spot while others merged together. Even though Vayssieres was able to get a dense array of ZnO nanowires on bare FTO, those results could not be repeated.

For denser wire growth, a ZnO thin film was used in place of nanoparticles as a seed layer. Unlike nanoparticles, the thin film completely coats the FTO and prevents any interaction between the FTO and solution, even after the growth of the wires. Figure 2.5 shows the results of a 50 mM growth. The thin film produced a highly ordered nanowire array with diameters of ~ 100 nm. All of the wires grew perpendicular to the substrate and have a hexagonal shape. This same array covered the entire substrate, 1 x 2 in., with an extremely small area of defects consisting mainly of unusually large wires. A Zinc foil substrate was also used because of the success of the thin film. With the foil, the thin thermal ZnO layer on the surface served as the seed layer, and the wire arrays grew similarly to the ZnO thin film, Figure 2.6.

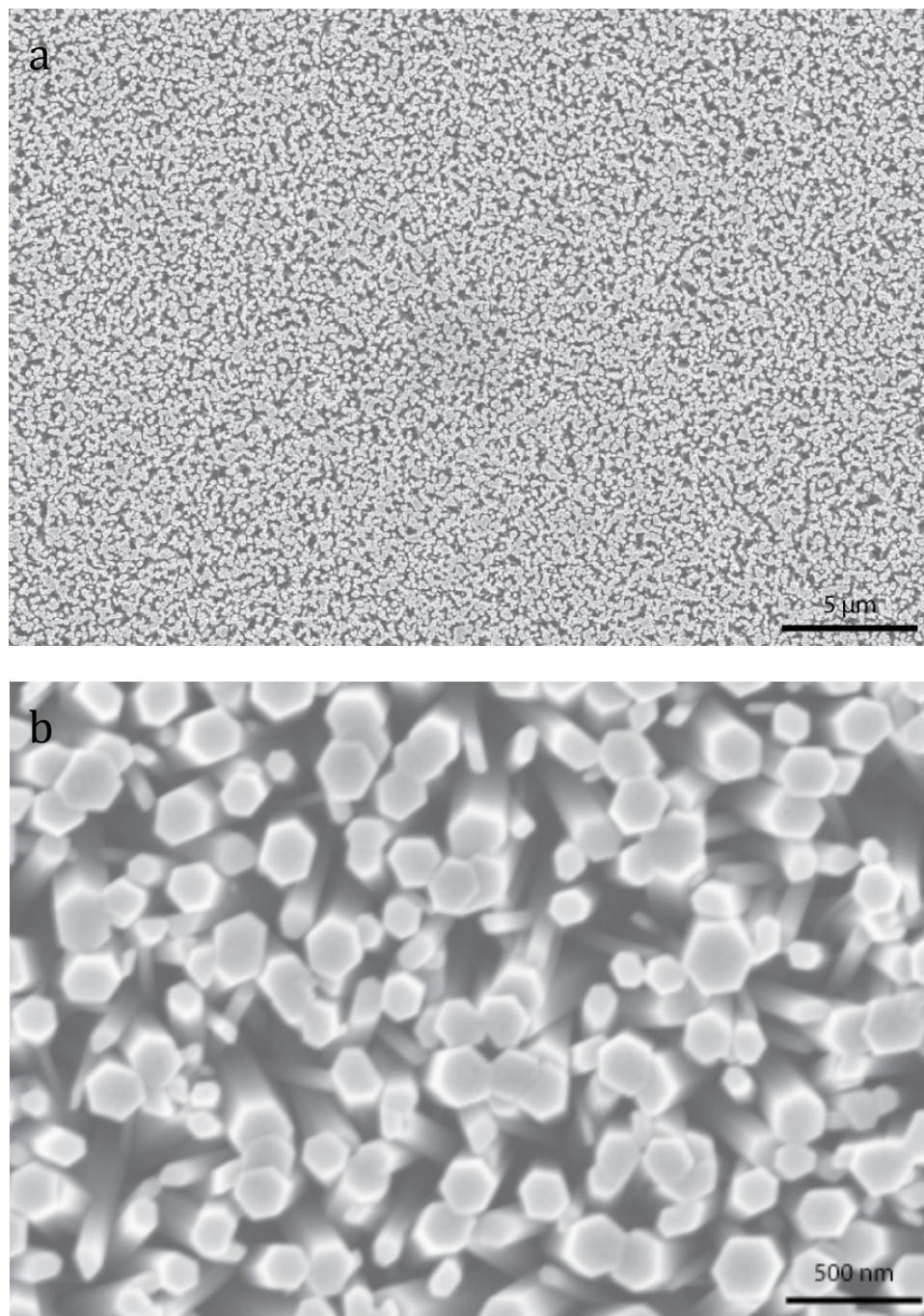


Figure 2.5: Nanowires on a thin film of ZnO on FTO grown from a 50 mM solution.

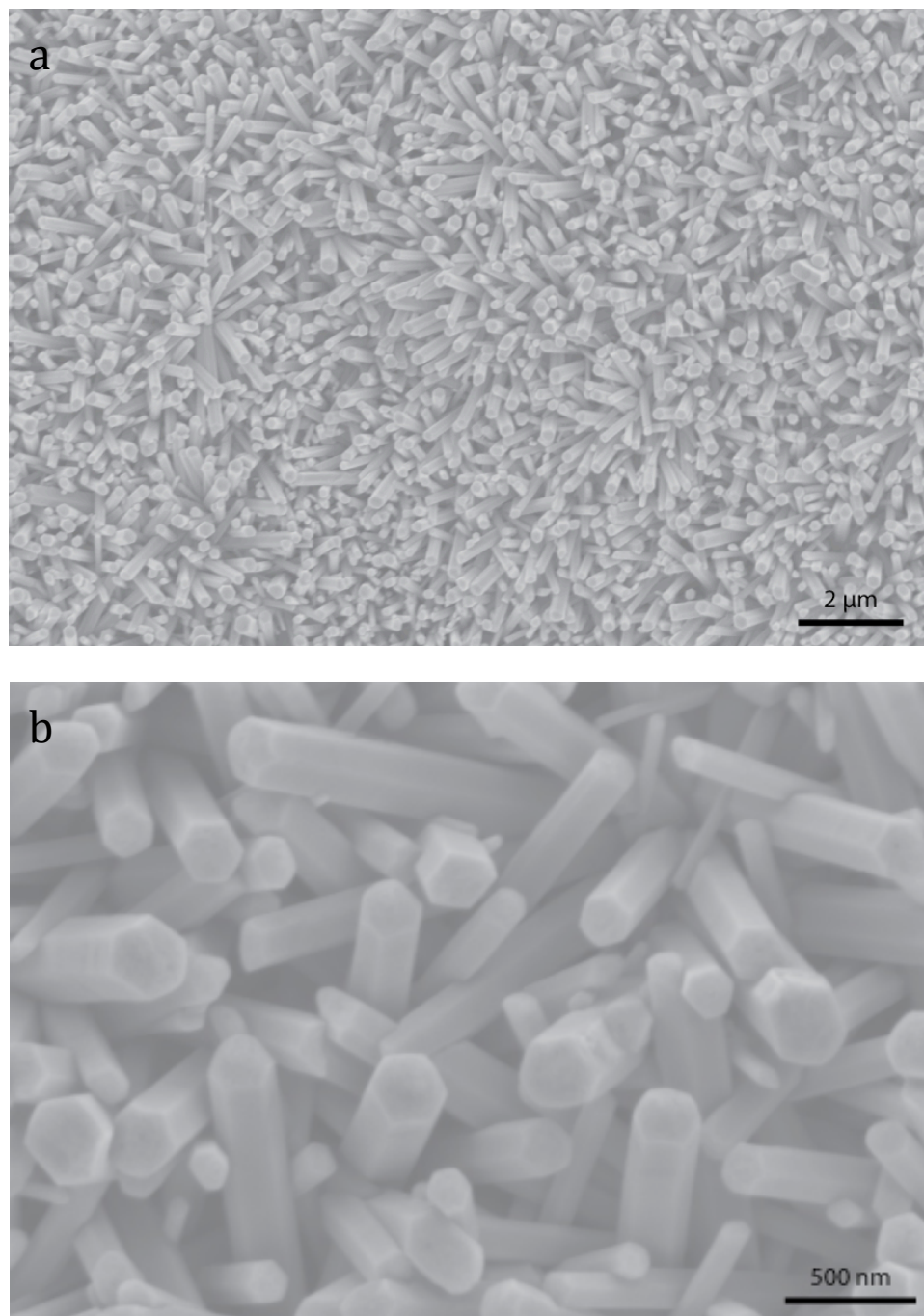


Figure 2.6: Nanowires on Zn foil grown from a 50 mM solution.

2.3.2 Time Dependence

Literature procedures for the nanowire arrays varied widely for the growth time and temperature, from 2 to 10 hours or more, and temperatures ranging from 80 °C to 95 °C. Therefore, the effect of time on nanowire growth was explored for three different substrates: FTO, ZnO thin film, and Zn foil. All growths were at 95 °C and from a 50 mM solution. Figure 2.7 displays the results from the FTO growth. During the first 2 hours the wires grew to lengths around 2 μm and diameters of ~ 800 nm, Figure 2.7a. At the 4-hour mark, the wires were 4 μm long and ~ 1 μm in diameter Figure 2.7b. After 4 hours, the wire growth stopped. At longer growth times, there was evidence of severe pitting and etching at the tips of the wires, Figures 2.7c-f.

The ZnO thin film showed the same result as the bare FTO with the growth stopping after four hours and etching occurring thereafter; however, the wires stopped at 2 μm with a diameter of only ~ 120 nm, Figure 2.8. This is significantly smaller than the FTO slide with 4 μm long and ~ 1 μm diameter wires, but the wire density is substantially higher with the ZnO thin film. The substrate clearly has an affect on the wire attributes. The effect corresponds with the wire density and as the density increases the average diameter and length decrease.

The Zn Foil typically produced wires with essentially the same attributes as the ZnO thin film. After 4 hours, the wire growth stopped, with lengths of 2 μm and diameters slightly bigger than the ZnO thin film at ~ 175 nm. However, one sample showed an entirely different behavior, Figure 2.9. The growth started the same and showed nanowires at 2 hours, but by the 4-hour mark, smaller wires started to grow

on the tops of the larger wires. This growth extended for over 18 hours and produced very fine structures. Previous reports on the growth of nanowires on pulsed laser deposited ZnO thin films produced the similar structures which were analyzed by TEM and found to be hollow nanotubes.¹⁴ The authors proposed that nanotube growth occurred on Zn terminated nanowires, while the normal wire growth continued to occur on the O terminated faces. The explanation was that the Zn termination caused a reduction in the Zn^{2+}/OH^- ratio, which encouraged tapering of the ends and seeded the growth of nanotubes. In my experiments, the nanotube growth was irreproducible and a reasonable explanation for the specific sample having a different nanowire termination could not be determined.

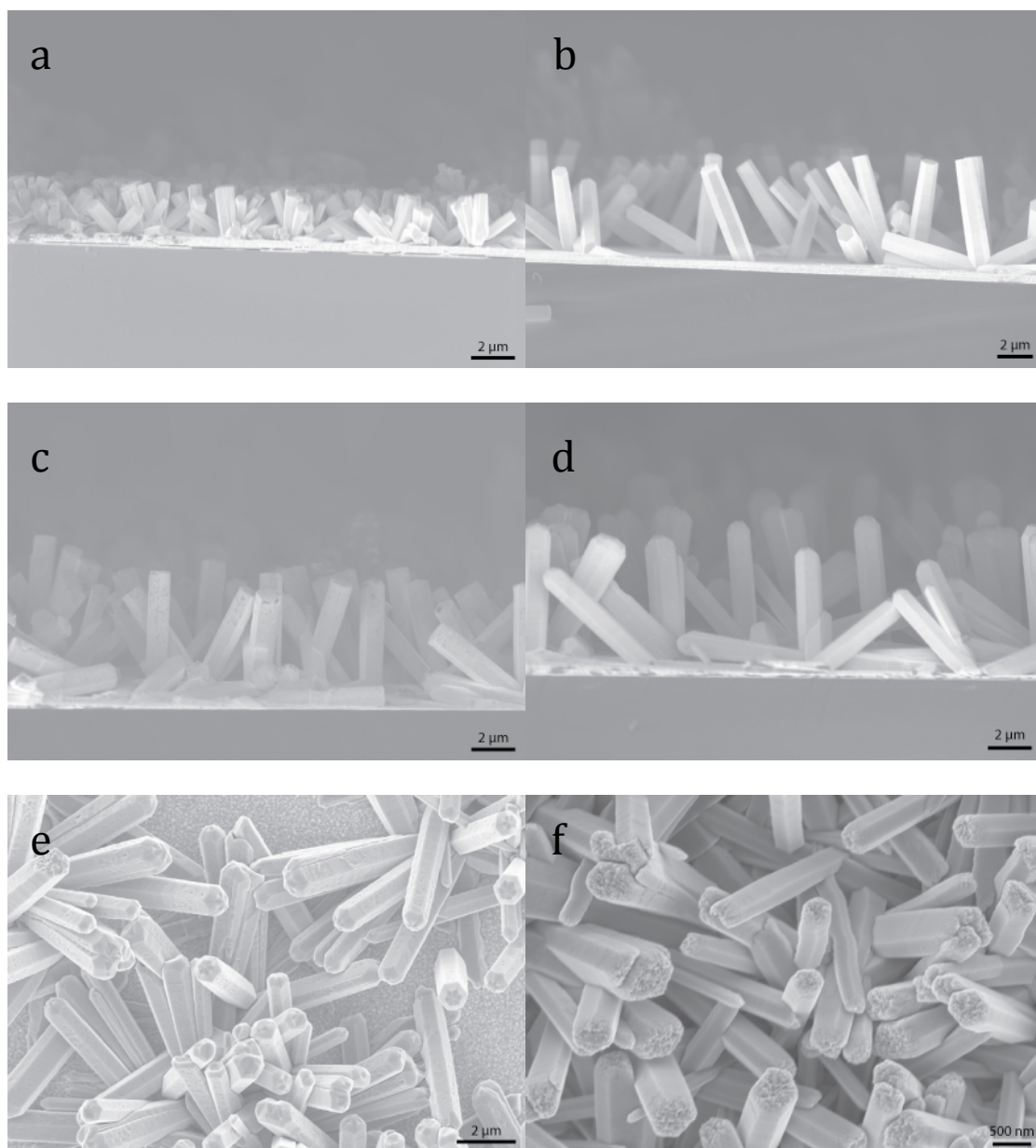


Figure 2.7: Time dependant study of nanowires on plasma cleaned FTO grown from a 50 mM solution. Side views of wires grown for 2 hrs (a), 4 hrs (b), 6 hrs (c), and 12 hrs (d). Top view of wires grown for 12 hrs (e) and 18 hrs (f).

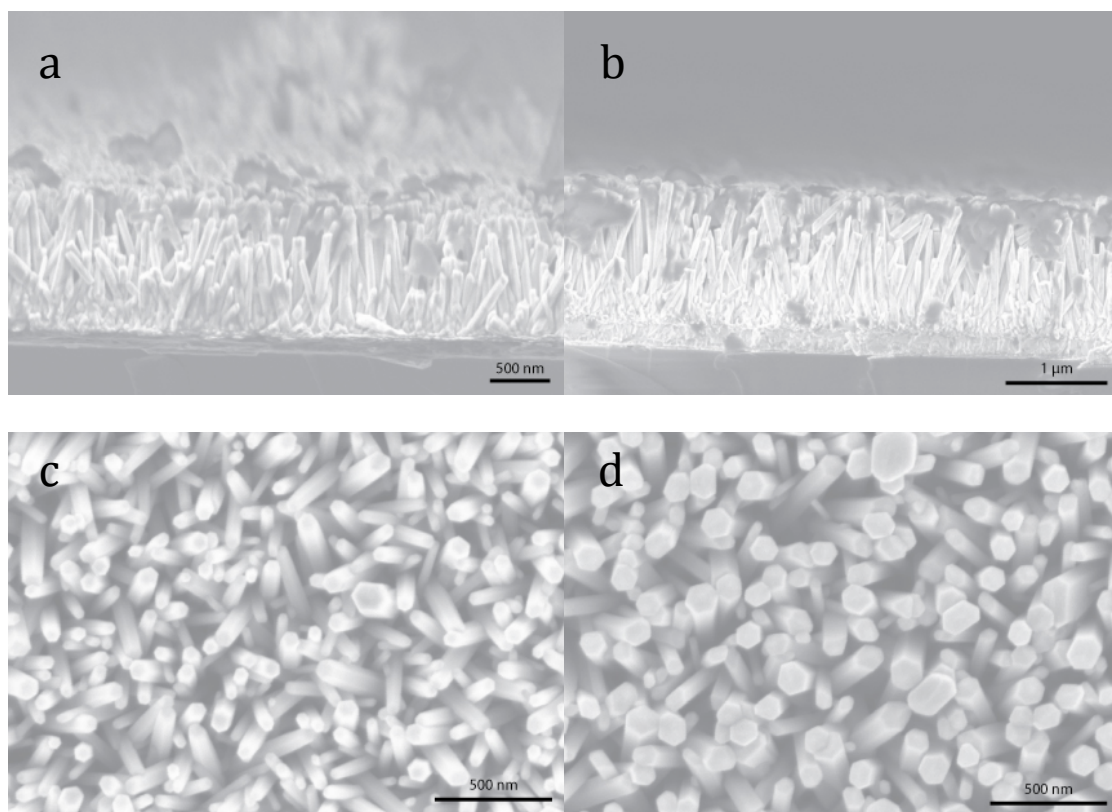


Figure 2.8: Time dependant study of nanowires on a thin film of ZnO on FTO grown from a 50 mM solution. Side view of wires grown for 2 hrs (a) and 4 hrs (b). Top view of wires grown for 2 hrs (c) and 4 hrs (d).

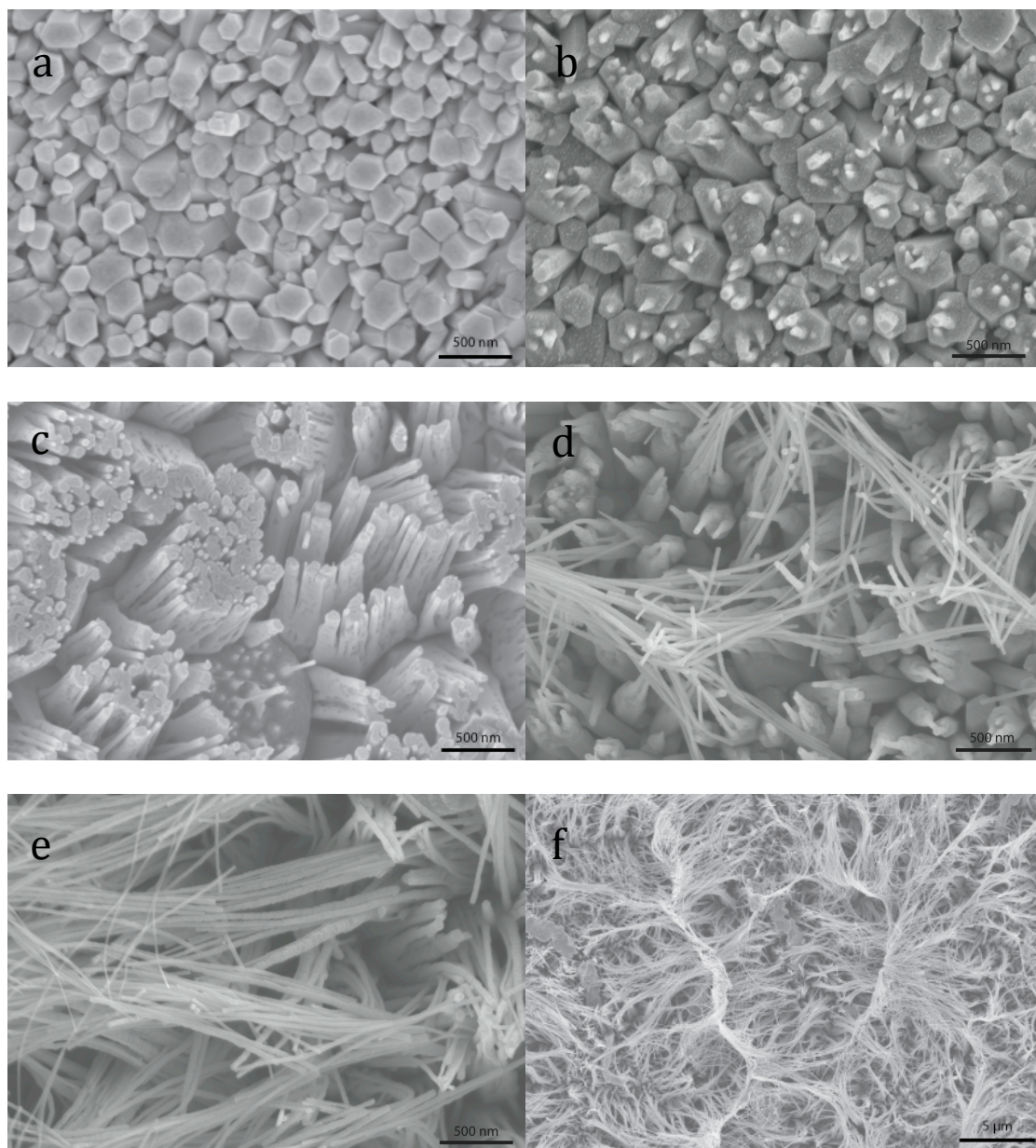


Figure 2.9: Irregular time dependant growth for nanowires on Zn Foil grown from a 50 mM solution. Top view for growth times of 2 hrs (a), 4 hrs (b), 6 hrs (c), 14 hrs (d) 18 hrs (e), and 18 hrs at a lower magnification (f).

2.3.3 Concentration Dependence

The length and diameter of the nanowires can also be affected by changing the solution concentrations. For nanowire growth, the zinc nitrate and hex still need to be in a 1:1 ratio, but decreasing both concentrations produces wires with smaller diameters. Figure 2.10 and 2.11 are the top and side views of ZnO nanowire arrays grown from a 5 mM, 25 mM, 50 mM, and 75 mM solution for 4 hours on a thin film of ZnO. The diameters increased with concentration, with diameters of 40 nm, 75 nm, 125 nm, and 300 nm respectively. The wire lengths for the 5 mM samples could not be determined because the small diameter wires fractured when the FTO slide was cut down to size. As for the 25 mM, 50 mM, and 75 mM the lengths were: 1.7 μm , 2.1 μm , and 2.8 μm respectively.

By increasing the concentration, the rates of the reactions 2.1 – 2.3 increase, as predicted by Le Chatelier's principle. This will increase the crystal growth on all faces, and while the (001) is still the fastest, there is an increase in the reaction velocity at all the faces, generating larger diameters. Thus, for the same growth time, wires with higher concentrations will have longer lengths and larger diameters as observed. This increase in reaction rate predicts larger wires; however, it does not predict changes in aspect ratio. The wires in the 25 mM, 50 mM and 75 mM have aspect ratios of 23, 17, 9 respectively indicating that the high concentration affect the diameter more than the length. A possible explanation is that at the point of nucleation, the higher concentrations generate bigger particles as seeds for the nanowire growth.

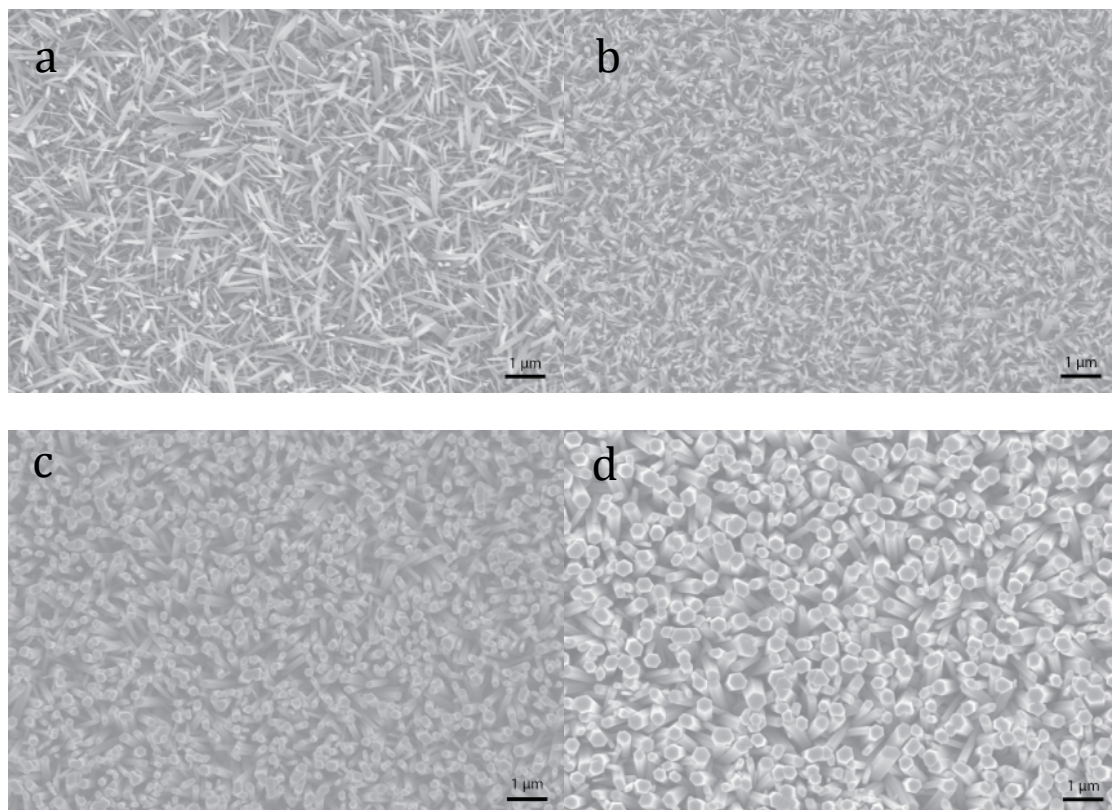


Figure 2.10: Concentration dependence for nanowires of a thin film of ZnO on FTO. Top view of 5 mM (a), 25 mM (b), 50 mM (c), and 75 mM (d) solution concentrations.

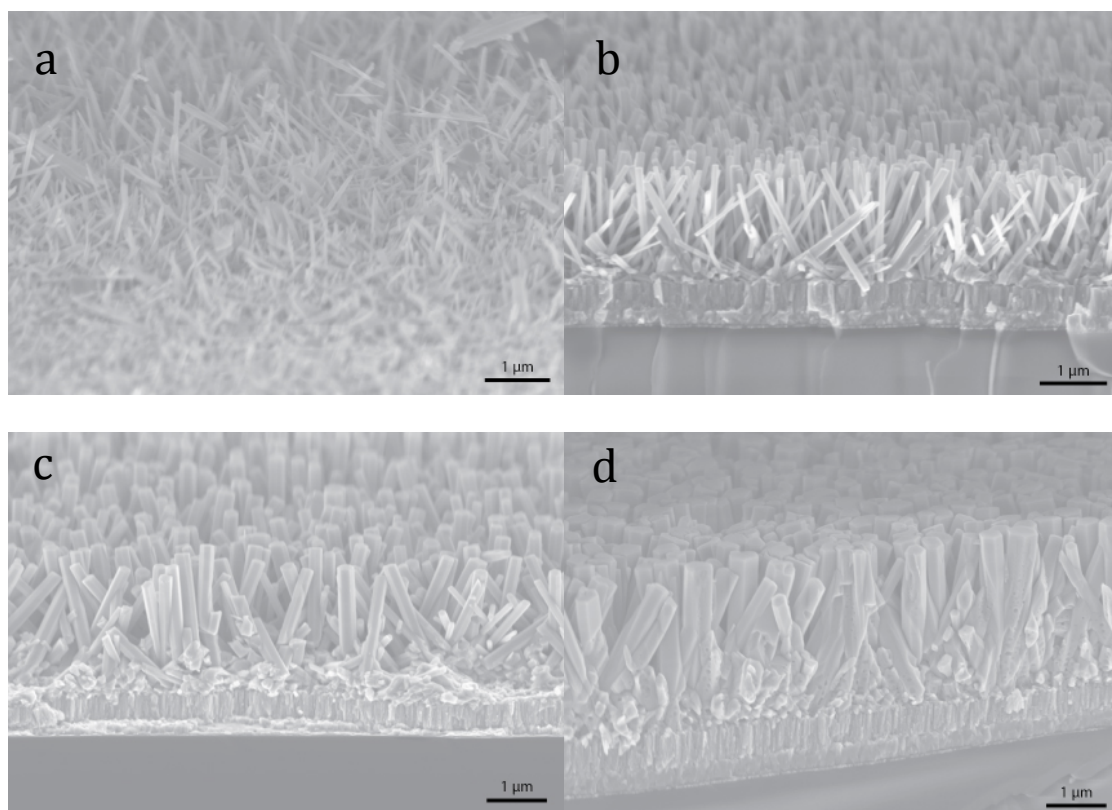


Figure 2.11: Concentration dependence for nanowires of a thin film of ZnO on FTO. Side view at 70° of 5 mM (a), 25 mM (b), 50 mM (c), and 75 mM (d) solution concentrations.

2.3.4 Extending the Wire Growth

After four hours, the electrode can be placed in a fresh solution and the growth continues. Figure 2.12 displays the images of a nanowire array grown on a thin film of ZnO from a 50 mM solution that was replaced after 4 hours and heated for an additional 4 hours. The extended growth doubles the length of the wires to 4.1 μm while the diameters increase slightly from 125 nm to 175 nm, when compared to Figures 2.8b and 2.8d, which are the wires after the initial 4-hour growth. For longer wire growth, a continuous flow reactor was setup with a peristaltic pump at a flow rate that replaced the solution every 3 hours. The results of a 110 hour growth from a 5 mM solution are seen in Figure 2.13, and the wires were 26 μm long and 250 nm in diameter. For a 50 mM solution, after just 36 hours of growth, the wires were 15 μm ; however, the majority of the wires had grown together, Figure 2.14.

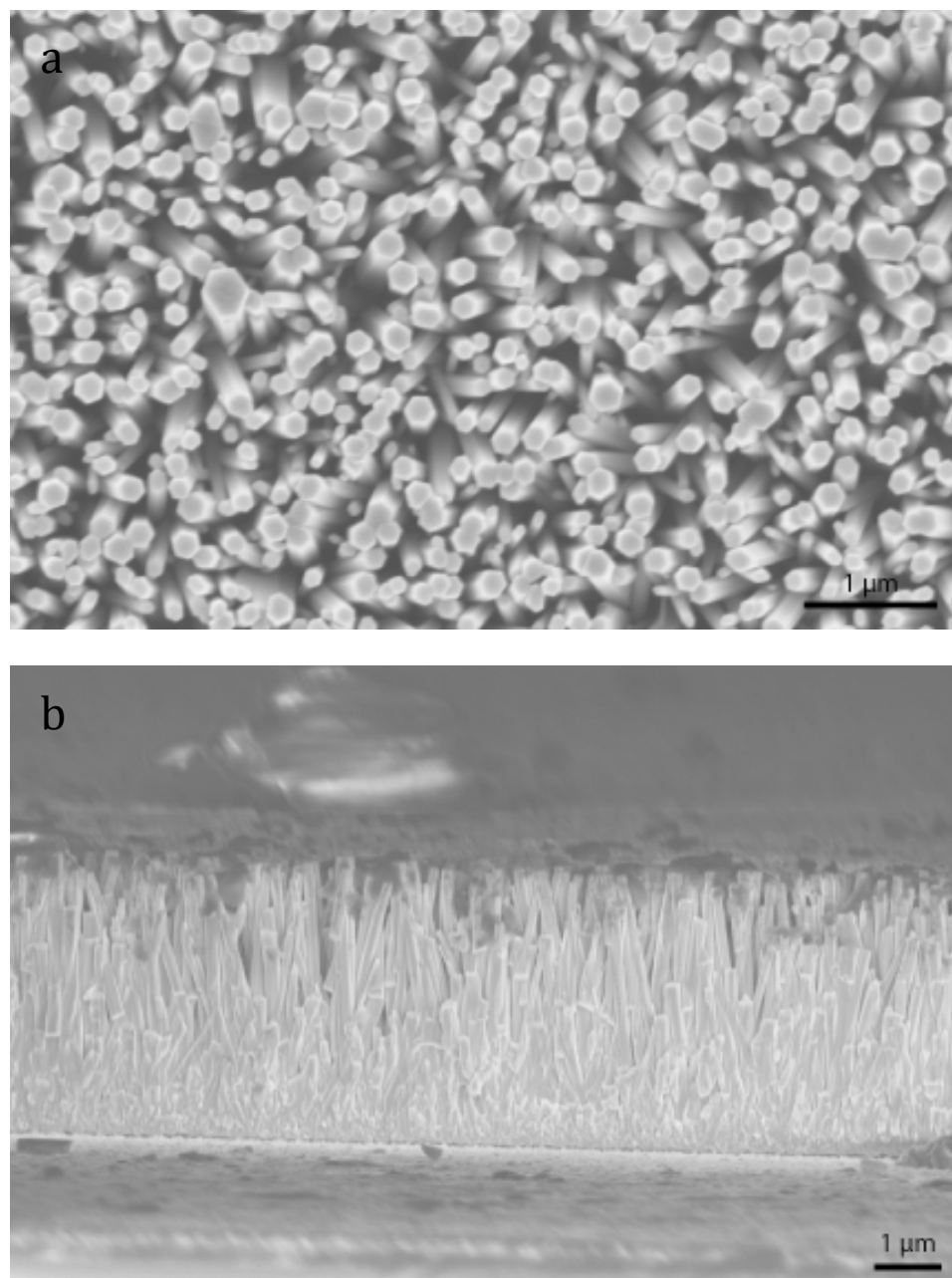


Figure 2.12: Extended growth for nanowires on a thin film of ZnO on FTO. The wires were grown from a 50 mM solution and the solution was replaced after 4 hrs and the growth was extended for an additional 4 hrs. Top view (a) and side view (b).

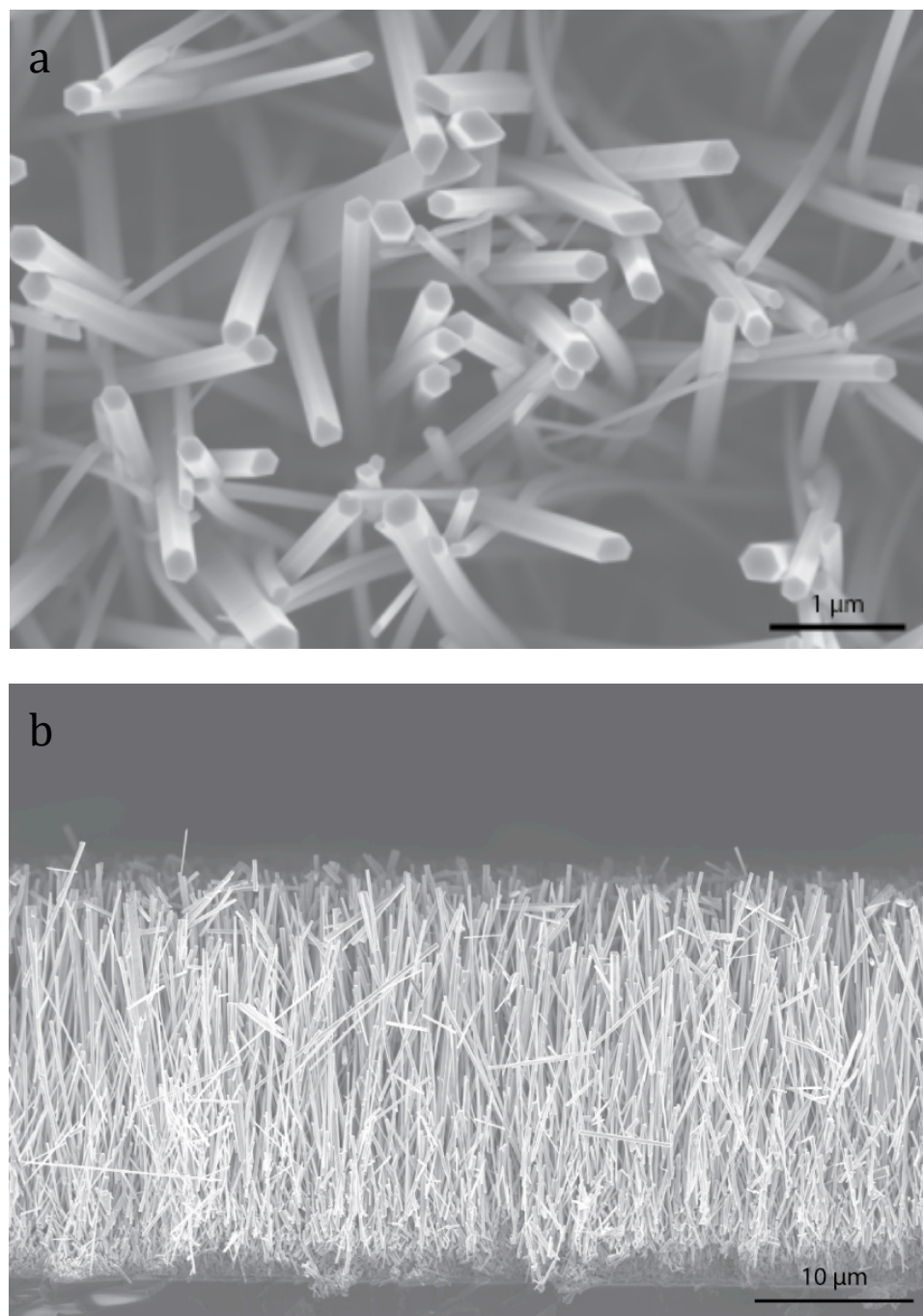


Figure 2.13: Nanowires on thin film of ZnO on FTO grown for 110 hrs in a continuous flow of a 5 mM solution with the solution replaced every 3 hrs. Top view (a) and side view (b).

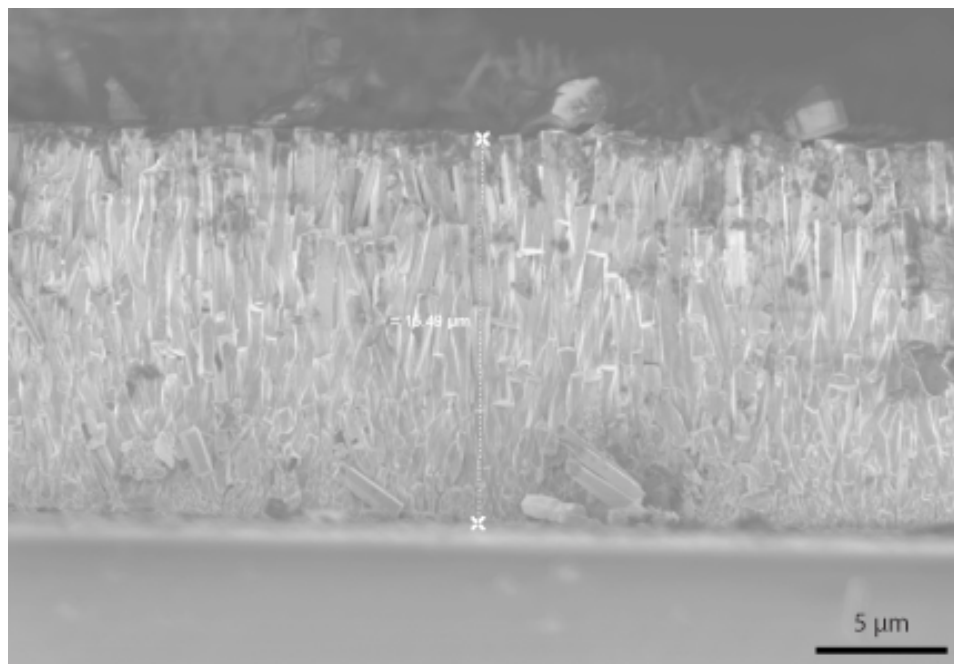


Figure 2.14: Nanowires on thin film of ZnO on FTO grown for 36 hrs in a continuous flow of a 50 mM solution with the solution replaced every 3 hrs.

2.3.5 Peeled Wire Arrays

The nanowire arrays can be removed from the substrate by encasing the wires in a polymer and peeling the wires off the substrate. This same method was used to remove silicon wire arrays.²⁰ Previous methods for removing the ZnO nanowires consisted of sonicating and dispersing the wires in methanol.^{21,22} This fractured the wires in random places and generated a solution of nanowire pieces. By encasing the wires in a polymer, the entire array can be removed without significantly fracturing the wires. Figure 2.15 is the SEM images of 4 μm and 20 μm length wire arrays with polydimethylsiloxane (PDMS) spin coated on the surface. In Figure 2.15a, there is a section where the film has already started to lift off the FTO, and it shows how easily the wires can be removed from the substrate. Only a completely transparent FTO slide remains after peeling the PDMS.

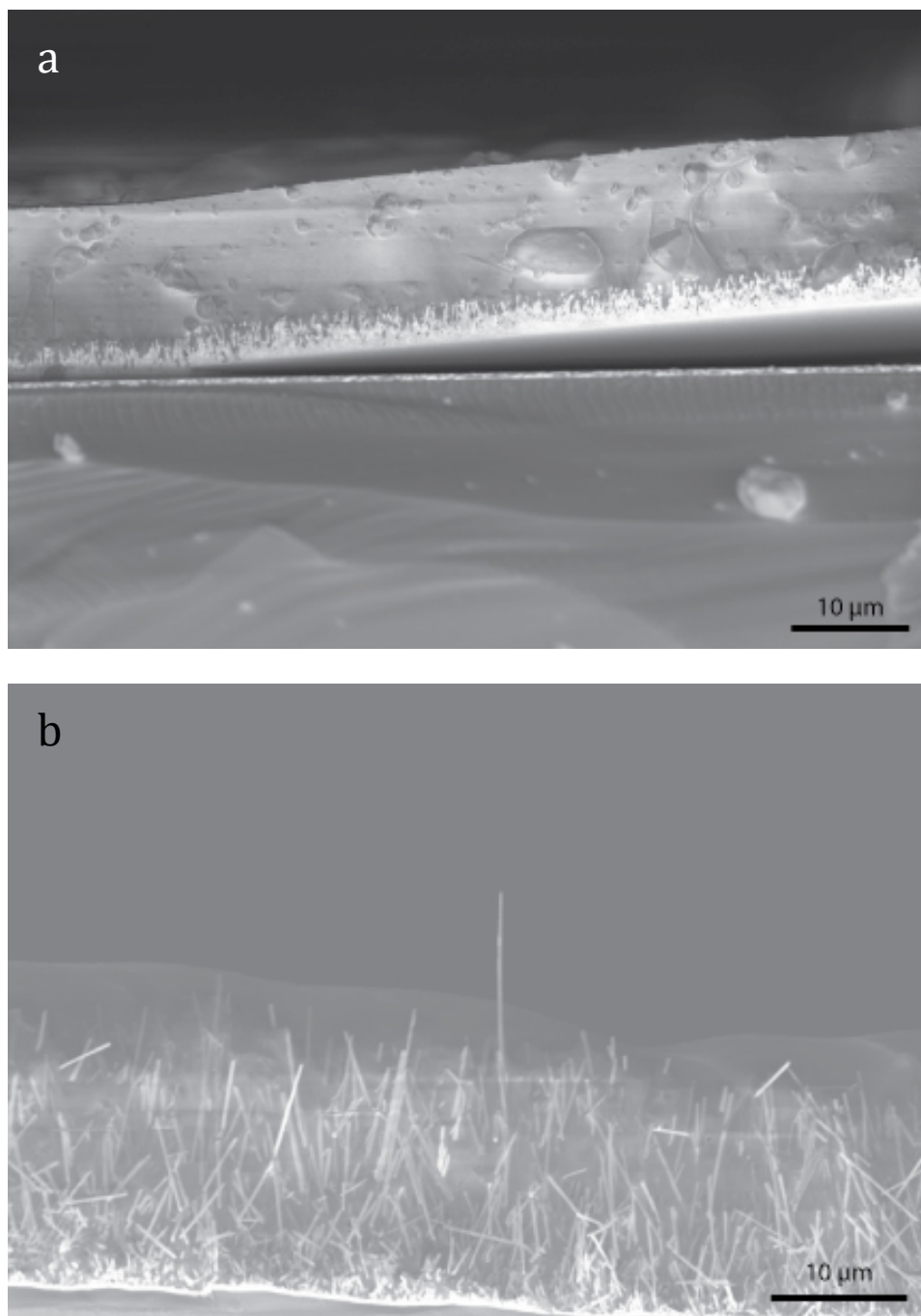


Figure 2.15: Short (a) and long (b) nanowire arrays encased in PDMS.

2.4 Discussion

From the results, the substrate can have a profound effect on the wire attributes. With bare FTO, different cleaning procedures produced different results, Figures 2.3 and 2.4. The density, length and diameters changed, even though all the other growth conditions were the same. The sparse wires from the plasma ashed FTO produced larger diameters and longer lengths for the same growth time as the dense arrays produced on the piranha cleaned FTO, ZnO thin film or Zn foil. There are two different explanations: one deals with the size of the seed particles, while the other deals with number of nucleation sites. For the seed particle theory, larger seed particles produce larger diameter wires and studies using different sized nanoparticles showed that small ZnO seed particles grew wires with smaller diameters.²³

The other theory depends on the number of nucleation sites. The difference in the wire attributes is a result of a difference in the local concentration of Zn^{+} . A high density of nucleation sites, in an unstirred solution, severely depletes the Zn^{+} concentration near the substrate. With the lower local concentration of Zn^{+} , growth will be slower producing smaller diameters and shorter lengths. In contrast, with only a few nucleation sites, the local Zn^{+} concentration will be higher, promoting faster growth and bigger wires. The authors demonstrated this effect by sputtering a thin film of ZnO on a silicon substrate and etching the ZnO for different times to reduce the thickness of the seed layer. As the etch time increased and the seed layer thickness decreased, the wires increased in diameter and length.

The density of nucleation sites explains the results obtained in this report. When comparing the results from the two different cleaning procedures for FTO, because both samples were grown on FTO, the seed particles are likely to be the same, Figures 2.3 and 2.4. The only difference was the density of wires, where the higher density on the piranha cleaned FTO produced smaller wires. Further support for the nucleation site explanation is the increase in length, which the seed particle theory does not support.

Both the growth time and solution concentration control the length and diameters of the wires. The dependence on concentration produced longer wires with bigger diameters at higher concentration, but the aspect ratio of the wires changed too. Higher concentrations produced short and fat wires, while lower concentrations produced tall and skinny wires. For the two data points with the growth time, 2 and 4 hours, the aspect ratio changed as well. At the longer growth times, the wires became taller and skinnier. From the images, it also appears that the size dispersion decreases, and this suggests that Ostwald ripening is occurring. This would explain the change in the aspect ratio with growth time, but unfortunately this was not confirmed.

In conclusion, the most reproducible method for nanowire synthesis uses the capped bottle setup with an oven as the heat source. A thin film of the ZnO serves as an excellent seed layer for high-density wire arrays. Using this substrate at 95 °C, growth stops after 4 hours at lengths around 2 μm . Growth can be extended by continually replacing the solution increasing the lengths to 30 μm or more. With the

conductive FTO and the protective thin film, these wire arrays are ready to be used in photoelectrochemical cells.

2.5 References

- (1) Look, D. C. *Materials Science and Engineering B-Solid State Materials for Advanced Technology* **2001**, *80*, 383.
- (2) Ozgur, U.; Alivov, Y. I.; Liu, C.; Teke, A.; Reshchikov, M. A.; Dogan, S.; Avrutin, V.; Cho, S. J.; Morkoc, H. *J. Appl. Phys.* **2005**, *98*.
- (3) Huang, M. H.; Mao, S.; Feick, H.; Yan, H. Q.; Wu, Y. Y.; Kind, H.; Weber, E.; Russo, R.; Yang, P. D. *Science* **2001**, *292*, 1897.
- (4) Yang, P. D.; Yan, H. Q.; Mao, S.; Russo, R.; Johnson, J.; Saykally, R.; Morris, N.; Pham, J.; He, R. R.; Choi, H. J. *Adv. Funct. Mater.* **2002**, *12*, 323.
- (5) Wang, Z. L. *Journal of Physics-Condensed Matter* **2004**, *16*, R829.
- (6) Huang, M. H.; Wu, Y. Y.; Feick, H.; Tran, N.; Weber, E.; Yang, P. D. *Adv. Mater.* **2001**, *13*, 113.
- (7) Vayssieres, L.; Keis, K.; Lindquist, S. E.; Hagfeldt, A. *J. Phys. Chem. B* **2001**, *105*, 3350.
- (8) Vayssieres, L. *Adv. Mater.* **2003**, *15*, 464.
- (9) Li, W. J.; Shi, E. W.; Zhong, W. Z.; Yin, Z. W. *J. Cryst. Growth* **1999**, *203*, 186.
- (10) Greene, L. E.; Law, M.; Goldberger, J.; Kim, F.; Johnson, J. C.; Zhang, Y. F.; Saykally, R. J.; Yang, P. D. *Angewandte Chemie-International Edition* **2003**, *42*, 3031.
- (11) Li, Q. C.; Kumar, V.; Li, Y.; Zhang, H. T.; Marks, T. J.; Chang, R. P. H. *Chem. Mater.* **2005**, *17*, 1001.
- (12) Tak, Y.; Yong, K. J. *J. Phys. Chem. B* **2005**, *109*, 19263.

- (13) Vayssieres, L.; Keis, K.; Hagfeldt, A.; Lindquist, S. E. *Chem. Mater.* **2001**, *13*, 4395.
- (14) Sun, Y.; Riley, D. J.; Ashfold, M. N. R. *J. Phys. Chem. B* **2006**, *110*, 15186.
- (15) Govender, K.; Boyle, D. S.; Kenway, P. B.; O'Brien, P. *J. Mater. Chem.* **2004**, *14*, 2575.
- (16) Pacholski, C.; Kornowski, A.; Weller, H. *Angewandte Chemie-International Edition* **2002**, *41*, 1188.
- (17) Jiang, L.; Li, G. C.; Ji, Q. M.; Peng, H. R. *Mater. Lett.* **2007**, *61*, 1964.
- (18) Jang, J. M.; Yi, S. H.; Choi, S. K.; Kim, J. A.; Jung, W. G. In *Advances in Nanomaterials and Processing, Pts 1 and 2*; Ahn, B. T., Jeon, H., Hur, B. Y., Kim, K., Park, J. W., Eds. 2007; Vol. 124-126, p 555.
- (19) Wang, J.; Cao, J. M.; Fang, B. Q.; Lu, P.; Deng, S. G.; Wang, H. Y. *Mater. Lett.* **2005**, *59*, 1405.
- (20) Plass, K. E.; Filler, M. A.; Spurgeon, J. M.; Kayes, B. M.; Maldonado, S.; Brunshwig, B. S.; Atwater, H. A.; Lewis, N. S. *Adv. Mater.* **2009**, *21*, 325.
- (21) Goldberger, J.; Sirbuly, D. J.; Law, M.; Yang, P. *J. Phys. Chem. B* **2005**, *109*, 9.
- (22) Park, W. I.; Kim, J. S.; Yi, G. C.; Bae, M. H.; Lee, H. J. *Appl. Phys. Lett.* **2004**, *85*, 5052.
- (23) Guo, M.; Diao, P.; Cai, S. M. *J. Solid State Chem.* **2005**, *178*, 1864.
- (24) Liu, J.; She, J. C.; Deng, S. Z.; Chen, J.; Xu, N. S. *J. Phys. Chem. C* **2008**, *112*, 11685.

Chapter 3

Comparison Between ZnO Nanowire Arrays and Single Crystals as Photoanodes for Water Oxidation

3.1 Introduction

Efficient and cost effective photoelectrochemical splitting of water into H₂ and O₂ is a major goal for inorganic chemists. Harnessing the sun's energy and directly storing it in chemical bonds provides a clean energy source that can be transported and used at anytime. Unfortunately, after more than 30 years, this process has not become feasible due to the cost, stability, and efficiency of current solar conversion devices. Part of the problem comes from the large voltage needed to split water, > 1.23 V. Using one photon to drive this reaction limits the overall efficiency based on the solar spectrum and severely limits the choice of semiconductor materials.¹⁻³ The band gap of the semiconductor must straddle both the water and H₂ potentials. Furthermore, this material must be stable for both oxidation and reduction of water.

Recently, there has been exploration in increasing the overall efficiency by using two photons to drive the reaction.^{2,4} With two photons, one semiconductor straddles the water potential while the other straddles the H₂ creating two photoelectrochemical cells. With two semiconductors, smaller band gap materials can be used and with varying band potentials. For overall water splitting, > 1.23 V

must be generated between the two cells. Furthermore, with the two-photon method, the cells can be broken up and optimized individually.

While the two-photon process can potentially increase the overall efficiency, the use of structured electrodes can further help to reduce cost. Structured electrodes, in particular wire arrays, remove the dependency of the absorption length on the minority carrier diffusion length.⁵ In a planar electrode, the thickness of the electrode is set to match the absorption length and therefore the excited carriers must be able to diffuse the entire thickness of the cell to be collected. For high collection efficiencies, the semiconductor needs extremely pure and crystalline in order to extend the lifetime of the photogenerated carriers. This introduces considerable cost to the device. In a wire array, the wires are long enough to absorb all the light, but the charges now have a shorter diffusion distance to the sides where they are collected. This has been theorized to significantly improve the efficiency of less expensive and lower quality semiconductor electrodes and has shown promising results.⁶⁻⁸

In this paper, the use of ZnO nanowire arrays will be explored as photoanodes for water splitting. ZnO was chosen because of the simple wet chemical synthesis for wire arrays.⁹⁻¹¹ With the large 3.3 eV band gap, ZnO has significant efficiency limitations, but will provide useful information on the use of structured electrodes as photoanodes for water splitting. ZnO wire arrays have been used in this cell before; however, to our knowledge, a comparison between the structured electrode and a planar electrode has not been explored.^{12,13} The goal of this paper is to compare the performance of the wire arrays to a single crystal and

explore the benefits and limitations of the structured electrode as well as the kinetics of ZnO as a photoanode for water oxidation.

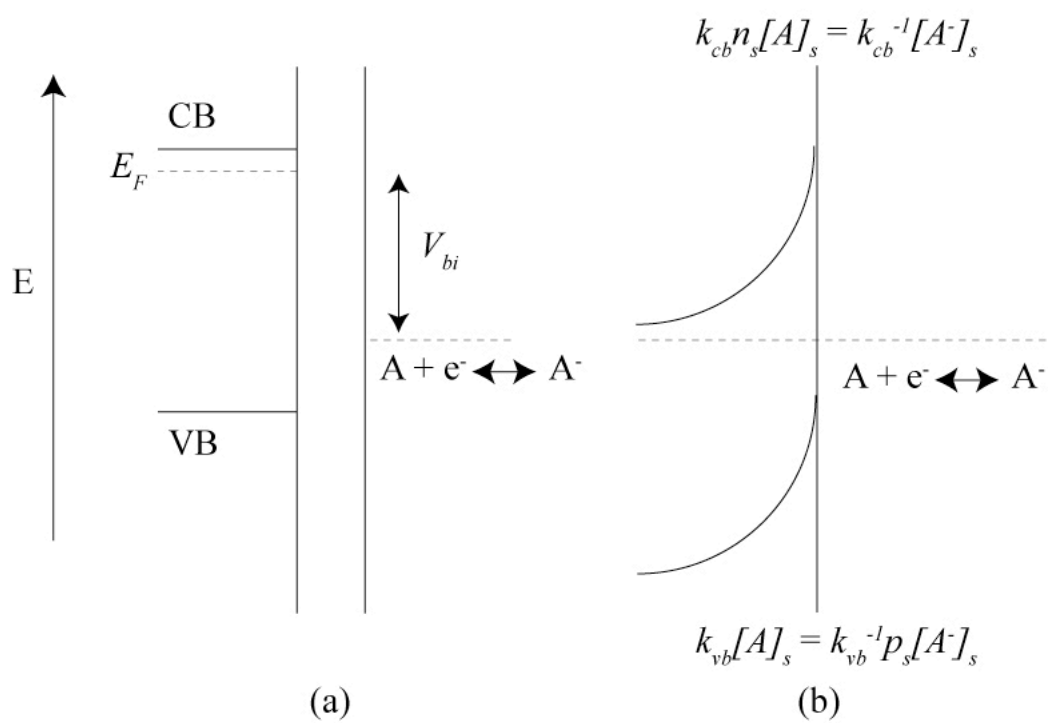
3.2 Background

Scheme 3.1 shows the energy diagram for an n-type semiconductor and a redox active solution, A/A^- , before contacting (a) and at equilibrium after contacting in the dark (b). Initially, when the semiconductor enters the solution, electrons will flow from the semiconductor into solution until the semiconductor Fermi level drops to the solution potential.¹⁴ The transfer of electrons leaves a net positive charge in the semiconductor and a negative charge in solution at the surface of the semiconductor. The energy bands in the semiconductor bend in response to the electric field at the interface, and the voltage difference between the semiconductor Fermi level and solution potential determines the amount of band bending. This difference is known as the built-in voltage, V_{bi} and represents the theoretical maximum attainable photovoltage for the cell.

After equilibration, there will be an equal flux of electrons into and out of the semiconductor. For n-type semiconductors in the dark, conduction band electrons generate current by the two rate expressions, equations 1 and 2. The rate of electron transfer into solution from the conduction band, \vec{K}_{CB} , is expressed in equation 3.1:

$$\vec{K}_{CB} = k_{cb}n_s[A]_s \quad (3.1)$$

where k_{cb} is the conduction band electron transfer rate constant, n_s is the surface



Scheme 3.1: Band Bending.

electron concentration and $[A]_s$ is the concentration of the acceptors at the surface of the semiconductor. The rate of electron injection into the conduction band, \bar{K}_{CB} , is expressed by equation 3.2:

$$\bar{K}_{CB} = k_{cb}^{-1} [A^-]_s \quad (3.2)$$

where k_{cb}^{-1} is the reverse reaction rate constant and $[A^-]_s$ is the concentration of the donors at the surface of the semiconductor. From equations 3.1 and 3.2, the current – voltage behavior in the dark is represented by equation 3.3:

$$J = -J_o \left[\exp\left(-\frac{qV}{kT}\right) - 1 \right] \quad (3.3)$$

where V is the voltage, J is the current density, J_o is the exchange current density, q is the charge on an electron, k is Boltzmann's constant, and T is the temperature. The voltage dependence arises from n_s , which varies exponentially with voltage.

Applying a negative voltage decreases the amount of band bending and therefore increases n_s . As more negative potentials are applied, the bands begin to unbend and current from equation 3.1 increases exponentially until reaching diffusion-limited current.

Under illumination, electron-hole pairs are generated within the semiconductor, and the number making it through the interface is $\phi\Gamma$ where ϕ is the quantum yield and Γ is the photon flux. Under normal solar applications, the number of electrons generated is insignificant compared to the concentration in the dark. Therefore, the photocurrent is carried by the valence band holes, and the rate expressions are in equations 3.4 and 3.5:

$$\bar{K}_{VB} = k_{vb} p_s [A^-]_s \quad (3.4)$$

$$\bar{K}_{VB} = k_{vb}^{-1} [A]_s \quad (3.5)$$

where \bar{K}_{VB} is the rate of holes going into solution, \bar{K}_{VB} is the injection of holes into the semiconductor, k_{vb} and k_{vb}^{-1} are the corresponding rate constants and p_s is the surface hole concentration in the valence band. Under illumination, the current generated by equation 3.4 ideally exists as an offset of the dark current from equation 3.3, and the total current can be calculated by equation 3.6:

$$J = J_{ph} - J_o \left[\exp\left(-\frac{qV}{kT}\right) - 1 \right] \quad (3.6)$$

where J_{ph} is the photocurrent density.

The open circuit voltage, V_{oc} , is the potential where the current from equation 3.6 equals zero and simplifies to equation 3.7.

$$V_{oc} = \frac{kT}{q} \ln\left(\frac{J_{ph}}{J_o}\right) \quad (3.7)$$

Both equations 3.6 and 3.7 assume that J_{ph} is independent of voltage, and at V_{oc} all the photogenerated carriers are collected. The net current goes to zero because at this potential the dark cathodic current from equation 3 is now equal to J_{ph} . This has been observed for semiconductors with fast interfacial kinetics and V_{oc} typically occurs a few hundred mV below V_{bi} where the majority of the photogenerated carriers are still being collected.

For water oxidation, the solution potential is determined by reactions 3.8 and 3.9. Both reactions produce O_2 from water, the only difference is whether H^+ ,



reaction 3.8, or OH^- , reaction 3.9, is involved in the reaction. Equation 3.8 has a standard reduction potential of 1.23 V vs NHE at a pH of 0 and 1 atm O_2 while equation 3.9 has a standard reduction potential of 0.40 V vs NHE at pH 14 and 1 atm O_2 . The potential dependence on pH is merely a Nerstian shift due to the changing H^+ and OH^- concentrations and predicts a 59 mV per pH unit shift in solution potential. For ZnO, and all metal oxides, there is also a 59 mV per pH unit shift in the band edges due to either a protonation and deprotonation of surface states or the intercalation of protons.¹⁵⁻¹⁷ The band edge shift directly coincides with the solution potential shift; therefore, the thermodynamics for water splitting does not change with pH. When ZnO is used as a photoanode, the photocurrent is generated by holes in the valence band oxidizing either H_2O or OH^- , while the dark current is the reduction of O_2 with electrons from the conduction band.

3.3 Experimental

Chemicals: Zinc nitrate hexahydrate 98% and hexamethylenetetramine 98%, were purchased from Aldrich. All chemicals were reagent grade or better and used as received. 18 M Ω cm resistivity water was used in all cases. ZnO single crystals with the (0001) Zn face were purchased from MTI Corporation.

Wire Growth: ZnO nanowire arrays were grown using the method of Vayssieres with slight modifications.¹⁸ A thin film of ZnO was used to seed the nanowire growth and increase the wire density. The thin film was deposited by

sputtering roughly 20nm of zinc metal (RF magnetron sputterer, Zn target of 99.99% purity from Kurt J. Lesker Company) onto a fluorine doped tin oxide (FTO) slide with part of the FTO masked to be later used for electrical contact. The zinc was thermally oxidized at 400°C for 2 hours under a continuous flow of air. After protecting the bare FTO with nail polish, the slides were placed diagonally in the aqueous growth solution with the seed layer face down. Wires were grown from either a 5 mM or 50 mM solution of ZnNO₃ and hexamethylenetetramine at 95°C for the specified time. For longer wire growth, the slide was placed in a fresh solution every 4 hours. Once the slides were cool, they were rinsed with water and the nail polish was removed with acetone. Annealed wire arrays were heated to 450°C for 1 hour in air.

Characterization: Electronic absorption spectra were measured using an Agilent 8453 UV-vis diode array spectrometer. X-ray Photoelectron Spectra (XPS) were collected with an M-Probe XPS system that has been described previously^{19,20}. Briefly, 1486.6eV X-rays, generated from an Al K α source, illuminated the sample from an incident angle of 35° off the surface. A hemispherical analyzer collected photoelectrons emitted along a trajectory of 35° off of the surface plane. All samples were sufficiently conductive so that no compensation for charging effects was required. X-ray diffraction spectra were obtained on a PANalytical X'pert pro diffractometer.

Photoelectrochemical Measurements: Nanowire electrodes were constructed by gluing a copper/tin wire to the back of the slide and using silver print to contact the bare FTO on the front side. The electrode was then sealed in white epoxy. Areas

of all electrodes were measured by digitizing photographs of a microruler and of the exposed electrode area. The single crystal was constructed in a similar fashion with In/Ga eutectic being used to make ohmic contact to the backside.

The working electrode was placed in a stirred aqueous 0.5M K₂SO₄ solution along with a platinum mesh counter electrode and saturated calomel electrode (SCE) as the reference. Light entered the cell through a pyrex window. All voltages are versus SCE unless noted otherwise. The pH of the solution was measured to be 6.4 with a Beckman pH meter. For pH 11 measurements, the pH was adjusted with a 0.1 M NaOH solution. A BAS100B potentiostat was used at a scan rate of 50 mV/s. The light source was either an Oriel Inc. solar simulator, with air mass (AM) 1.5 filters and at 100mW/cm², or a 200W mercury lamp with a 365 nm mercury line filter with 5 nm FWHM spectral window.

Spectral Response: The spectral response of the electrodes in pH 11 - 0.5 M K₂SO₄ was measured with a home-built setup. The light source was a 75 W Xe lamp with a Cornerstone 260 1/4m dual grating monochromator. Current was measured every 5 nm at an applied potential of 350 mV vs SCE. The quantum yield was determined by comparing the response to a calibrated photodiode from UTD Sensors Inc. that was calibrated every 10 nm from 200 nm to 1100 nm and then interpolated to get a 5 nm resolution.

3.4 Results

3.4.1 Growth Conditions

A controlled precipitation process developed by Vaysseries was used to make the ZnO wire arrays.¹⁸ With this method, wires grow perpendicular to the substrate from an aqueous solution of ZnNO₃ and hexamethylenetetramine heated to 95 °C for a specified time. This method allows for control over both the length and diameter of the nanowires by varying the solution concentration and time respectively.^{10,18} Using a thin film of ZnO as a seed layer for rod growth, dense nanowire arrays were grown on FTO. The concentration of the zinc nitrate and hexamethylenetetramine, while still in a 1:1 molar ratio, controlled the diameter of the wires where a decrease in concentration decreases the average diameter.

SEM images of a 5 mM and 50 mM growth are shown in Figure 3.1a-d. The average diameter for a 4 hour growth time at 95 °C in the 5 mM and 50 mM solutions are ~ 40 nm and ~ 125 nm, respectively. It was found that the wire growth stopped after 4 hours, at 1.4 μm for the 5 mM and 2.1 μm for the 50 mM. Growth continued with a fresh solution, and heating for additional 4 hours increased the wire length for the 50 mM solution to 4 μm, Figures 3.1e and 3.1f. The second growth resulted in the rods doubling in length but increasing only slightly in diameter to an average of ~ 175 nm in the 50 mM solution.

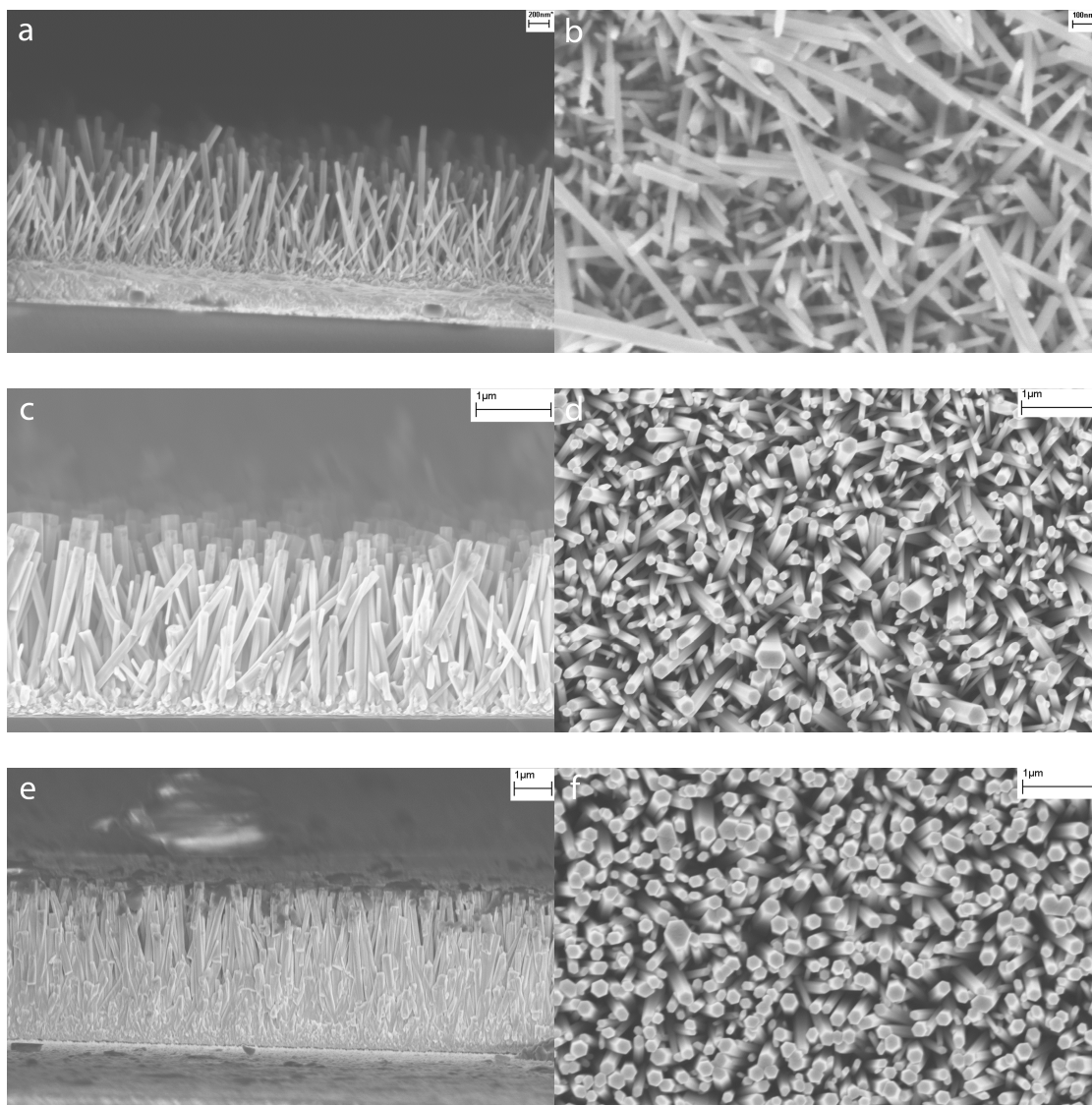


Figure 3.1: SEM images of the side and top view of ZnO nanorods grown from a: 5 mM solution for 4 hrs (a, b), 50 mM solution for 4hrs (c, d), and a 50 mM solution for 4 hrs followed by 4 hrs in a fresh 50 mM solution (e,f).

3.4.2 Characterization

ZnO wire arrays grown by this method are highly crystalline with the wurtzite crystal structure, Figure 3.2. Annealing the wires for two hours at 450°C under air, showed essentially no difference in the XRD spectra, Figure 3.2. The rods grow along the (0001) axis and are roughly perpendicular to the substrate.^{10,18} There is an expected elongation of the (002) peak due to the orientation of the nanowires.

The UV-vis spectra of 2 μm long wires, grown from a 5 mM solution, can be seen in Figure 3.3. The absorbance near the 3.3 eV band gap is above 1 indicating that the wires are long enough and dense enough to absorb a significant portion of the incident light. Unfortunately, the 50 mM arrays scattered too much light, due to the larger diameters, for transmission measurements. It is assumed the absorbance spectra of these films is similar to the 5 mM if not higher due to the denser rod growth of the 50 mM as seen in the SEM images, Figure 3.1.

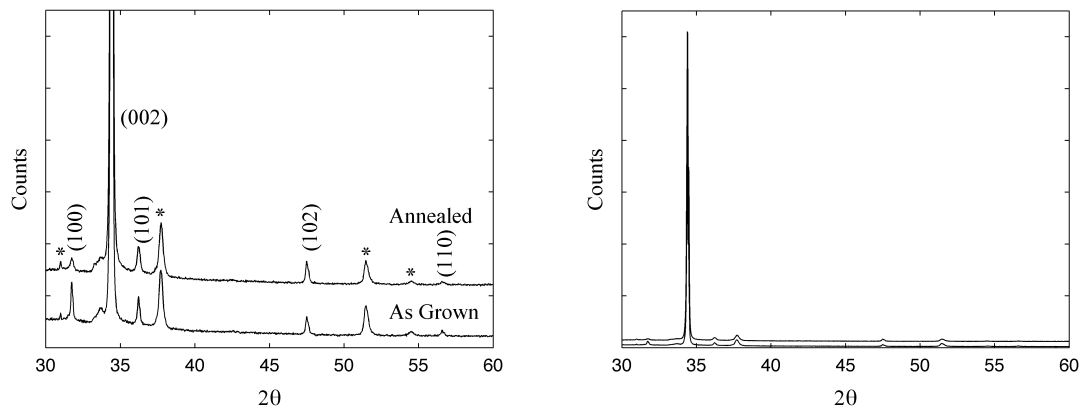


Figure 3.2: XRD of the ZnO nanowire films as grown and after annealing at 450 °C for two hours in air. The asterisk indicates peaks from the FTO.

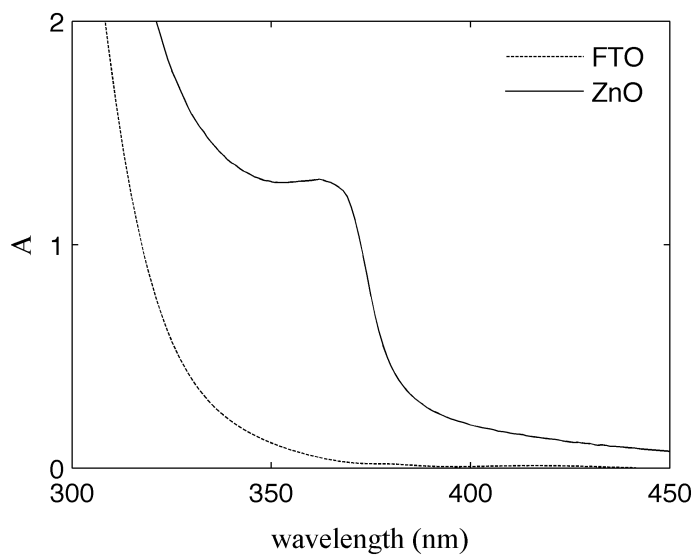


Figure 3.3: Absorbance spectra of the 5 mM ZnO nanowires.

3.4.3 Water Oxidation Results

Single Crystal: ZnO single crystals served as the planar comparison for the nanowire arrays. With the availability of high quality ZnO single crystals, commercial samples have long minority carrier diffusion lengths and exhibit a high efficiency for water oxidation. In previous ZnO electrochemical measurements, etching the electrode in a wide variety of acids or a Br₂-methanol solution conditioned the surface.^{21,22} The effect of etching in 1 M H₃PO₄ and 1 M H₂SO₄ on the photocurrent is in Figure 3.4. Both of the curves do not follow the behavior predicted by equation 3.6. The photoanodic current reaches a relatively constant current at 0 V as predicted by equation 3.6, but the cathodic current never increases exponentially. At potentials near V_{oc} both the cathodic and anodic currents are small. This premature decrease in current is indicative of non-ideal interfacial kinetics resulting in an overpotential for electron transfer at the semiconductor surface.²³

When comparing the different etches, H₃PO₄ has a significant reduction in current, while the V_{oc} extends out to more negative potentials than the H₂SO₄ etch. The measured V_{oc} for the H₃PO₄ etch was -608 mV while the H₂SO₄ was only -466 mV. Even though the H₃PO₄ etch has a higher V_{oc} , the power area is significantly smaller because the current dies off at essentially the same potential as the H₂SO₄ etch. The loss in current and increase in V_{oc} for the H₃PO₄ is likely due to surface bound phosphate groups decreasing the rate constant for electron transfer at the semiconductor interface. Upon etching, both phosphate and sulfate groups can attach themselves to the ZnO surface. Sulfate binding to metal oxide surfaces is

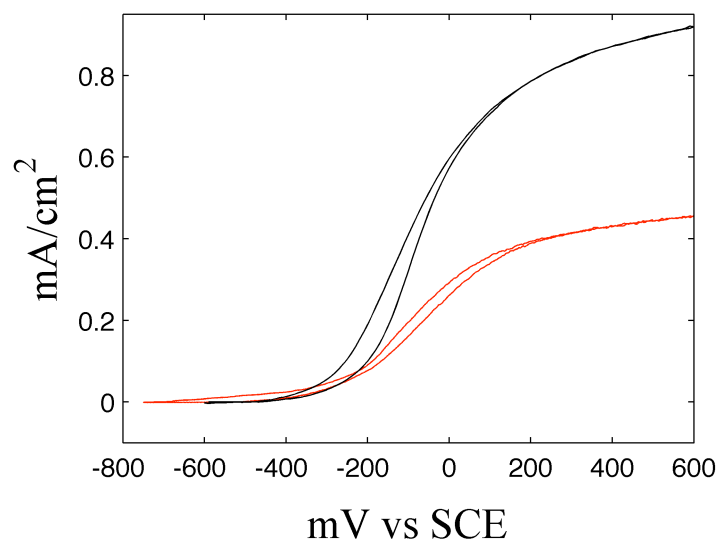


Figure 3.4: AM1.5 response of ZnO single crystals in 0.5 M K_2SO_4 at pH 6.4. Black curve was etched in H_2SO_4 where the red curve was etched in H_3PO_4 .

unstable in aqueous solutions, but the phosphate groups are stable.^{24,25} This surface adsorbed layer acts as a barrier to electron transfer as either a potential barrier or increased charge transfer distance. Therefore, the H₂SO₄ etching of the single crystal was used in all comparisons with the nanowire arrays.

ZnO Nanowire Arrays: In order to compare the wire arrays to the single crystal, the optimal growth conditions for maximum performance needed to be determined. First of all, it is important that the wires produce the majority of the photocurrent and not the thin ZnO film used to seed the wire growth. As can be seen from Figure 3.5, there is negligible current produced by the thin film. Also shown in Figure 3.5 is the effect of annealing the wires grown from a 50 mM solution. The annealed wire arrays show an improved performance in both current and voltage. This is surprising considering that there was no difference in the XRD spectra of the two wire arrays. Annealing also improved the performance of ZnO nanowire arrays in dye sensitized solar cells.²⁶

From the two different growth solutions, 5 mM and 50 mM, with a 4-hour growth time, the 5 mM wires were unstable and the photocurrents quickly degraded, while the 50 mM wires were able to maintain photocurrents under continuous running for 3 hours. The main difference in the two samples is the wire diameter. For the 5 mM wires, the diameter is only 40 nm and therefore the depletion width can only be 20 nm while the 50 mM wires can have depletion widths as long as 60 nm. With the shorter depletion width in the 5 mM wire arrays, the small amount of band bending was unable to prevent the degradation of the ZnO.

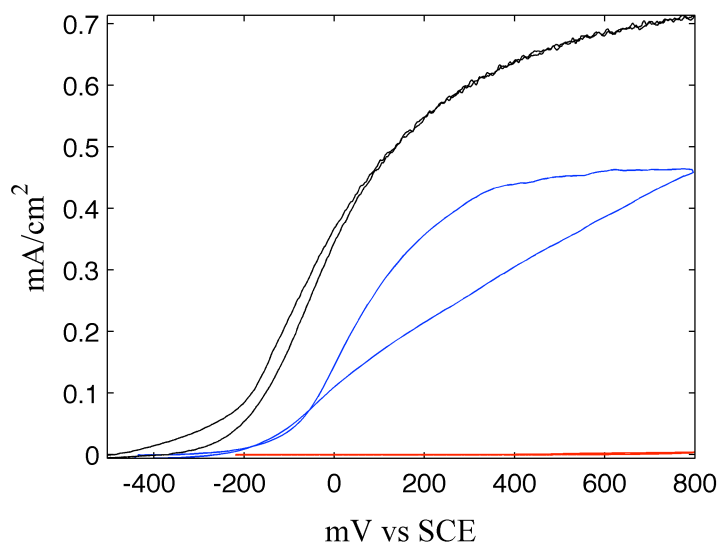


Figure 3.5: Photoresponse of the as grown nanorods (blue), annealed nanorods (black) and the 20 nm ZnO seed layer (red) to 365 nm light.

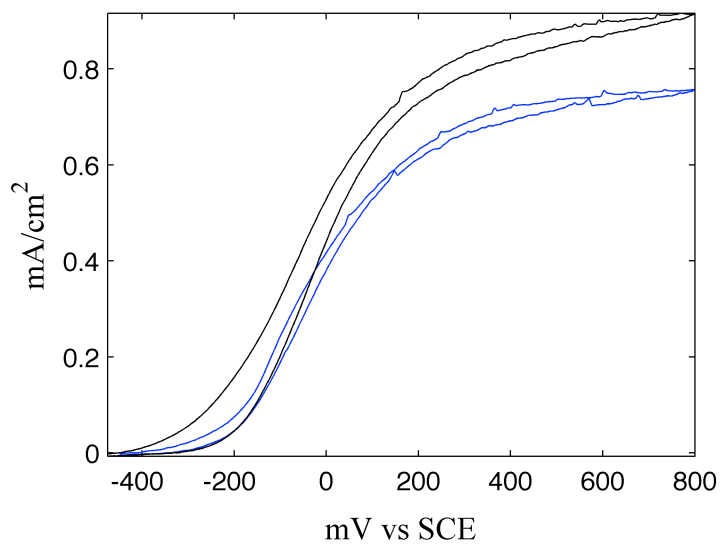


Figure 3.6: 365 nm photoresponse of 2 μm (blue) and 4 μm (black) length wire arrays in 0.5 M K₂SO₄ at pH 6.4.

For the 50 mM solution, extending the growth for an additional 4 hours in a fresh solution increased the wire length from 2 μm to 4 μm and showed a significant increase in photocurrent for near band gap illumination, Figure 3.6. This was unexpected considering the high absorbance values of the 2 μm long 5 mM wires, Figure 3.3, and the higher density of the 50 mM wires, Figure 3.1. The increase in current could be due to the difference in the wire diameters and longer depletion width. The longer depletion width, 85 nm, creates a larger electric field, better charge separation and higher quantum yield.

From these results, the optimized wire arrays were found to be grown from a 50 mM solution at 95 $^{\circ}\text{C}$ for 4 hours followed by an additional 4 hours in a fresh solution, Figures 1e-f, and were annealed in air at 450 $^{\circ}\text{C}$ for 2 hours.

Planar vs Wire Arrays: By comparing the optimized wire arrays to a single crystal provides a performance bench mark and the effect of the high surface area can be examined. Figure 3.7 displays the AM1.5 responses and the dark responses of the single crystal and wire arrays in 0.5 M K_2SO_4 . The dark curves for both electrodes show essentially no cathodic current even after the photocurrent died off. This is not too surprising when considering the low O_2 concentration, ~ 0.3 mM, in air saturated water. The low concentration and poor kinetics result in the low limiting cathodic currents.

For the light responses, both of the electrodes have essentially the same performance with a V_{oc} of -466 mV and -474 mV for the single crystal and wire array

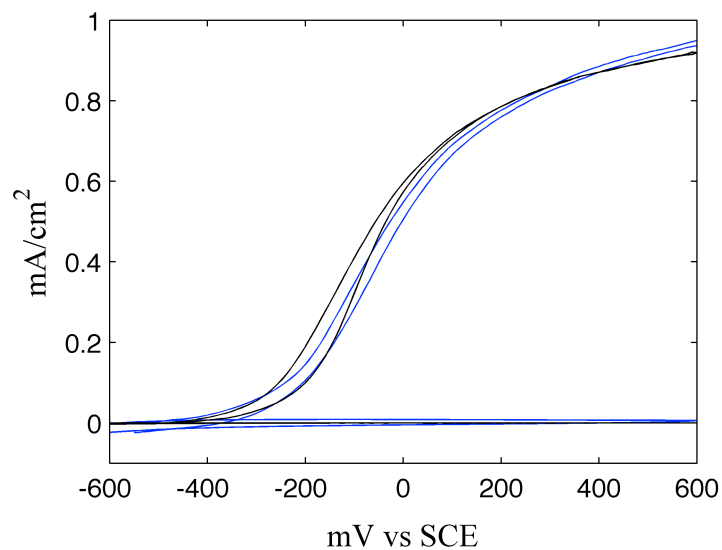


Figure 3.7: AM 1.5 light and dark curves of the single crystal (black) and 4 μm length wire arrays (blue) in 0.5 M K₂SO₄ at pH 6.4.

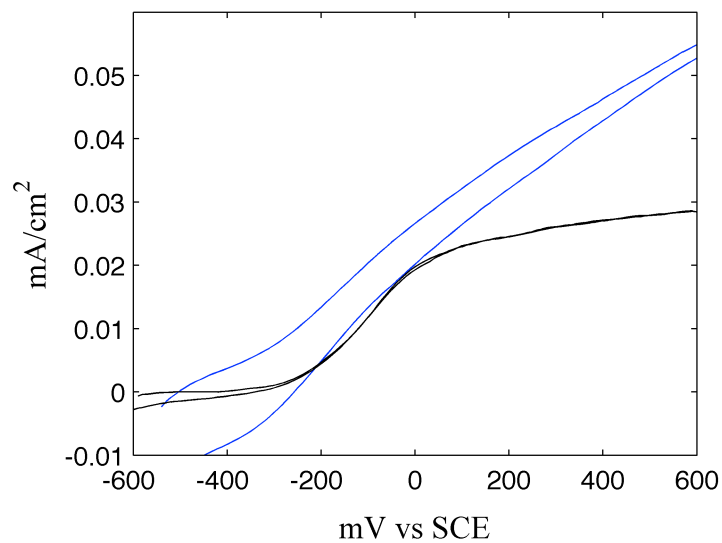


Figure 3.8: AM 1.5 with 385 nm long pass filter photoresponse of single crystal (black) and 4 μm length wire arrays (blue) in 0.5 M K₂SO₄ at pH 6.4.

respectively. The current is essentially the same for the both electrodes and dies off significantly before V_{oc} . Accurate values of the short circuit current density, J_{sc} , could not be determined because the solution potential is unknown. O_2 is not at 1 atm and with the near neutral pH, the passage of current causes significant changes in the solution potential. Buffers were not used because inorganic buffers, like phosphates, would bind to the surface while organic buffers would act as an additional acceptor for holes from the valence band. The pH was monitored during these measurements and replaced if the pH shifted by more than 1.5 units.

With a 385 nm long pass filter, the performance of the wires differs from the single crystal, Figure 3.8. Curves for the single crystals have essentially the same shape, while the response of the wires is more linear. Even with the linear behavior, the wires generate more current with the longer wavelength light and higher voltages, -386 mV vs -310 mV for the nanowires and single crystal respectively.

pH 11 with bubbling O_2 : By moving to a pH with a significant concentration of OH^- and bubbling O_2 at 1 atm, the solution potential can be calculated. For pH 11 the solution potential is 337 mV vs SCE. Figure 3.9 and Table 3.1 display the performances of the ZnO nanowire arrays and single crystal in this electrolyte. The J - V response is noticeably different than the results at pH 6.4. First of all, the photoanodic current extends to more negative voltages, which is expected due to the shift in the solution and band edge potentials. There was also a change in the shape of the light and dark J - V curves. The main difference in the shape of the light response is near V_{oc} , where there is significantly more current at pH 11.

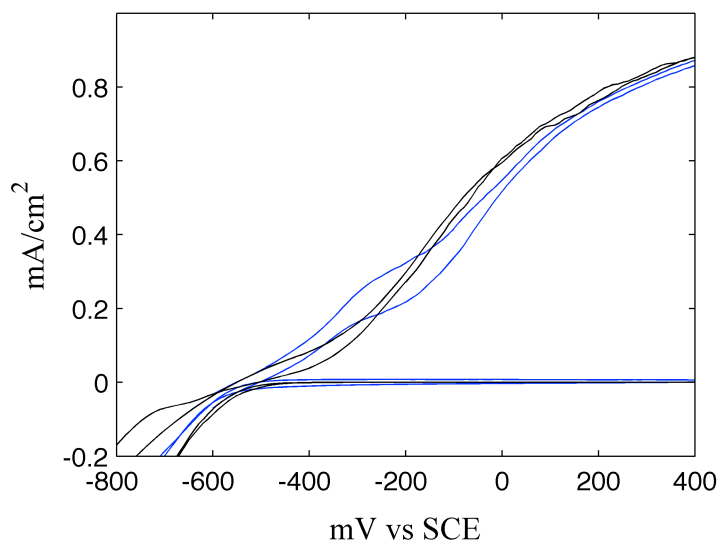


Figure 3.9: AM 1.5 light and dark curves of ZnO single crystal (black) and 4 μm length wires (blue) in 0.5M K_2SO_4 pH 11 with O_2 bubbling.

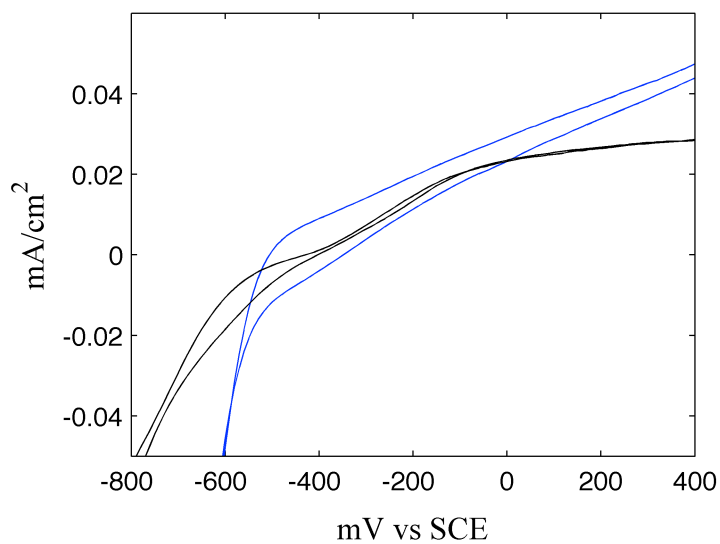


Figure 3.10: AM 1.5 with 385 nm long pass filter photoresponse of single crystal (black) and 4 μm length wires (blue) to in 0.5M K_2SO_4 pH 11 with O_2 bubbling.

	4 μm Length Wires	Single Crystal
J_{SC} (mA/cm ²)	0.827	0.866
V_{OC} (mV) vs cell	886	910
ff	0.25	0.28
eff	0.18	0.22

Table 3.1: AM 1.5 response for ZnO single crystal and 4 μm length nanowire arrays in 0.5 M K₂SO₄ at pH 11 with O₂ bubbling.

	4 μm Length Wires	Single Crystal
J_{SC} (mA/cm ²)	0.044	0.022
V_{OC} (mV) vs cell	800	836
ff	0.28	0.40

Table 3.2: AM 1.5 with 385 nm long pass filter response for ZnO single crystal and 4 μm length nanowire arrays in 0.5 M K₂SO₄ at pH 11 with O₂ bubbling.

When examining the dark currents, there is also an increase in current near V_{oc} , especially for the wire arrays. From Figure 3.7, in pH 6.4 the dark cathodic current is limited to a current density less than $5 \mu\text{A}/\text{cm}^2$. By switching to pH 11 and bubbling O_2 , the current density increases faster and to higher limiting currents, especially for the wire arrays, but the increase in dark current remains at potentials past V_{oc} and does not approach J_{sc} .

From Table 3.1, the efficiency of the single crystal slightly exceeds the wires, 0.22 % for the single crystal versus 0.18 % for the wire arrays. The higher efficiency is from the single crystal generating slightly more current and voltage with a higher fill factor than the wire arrays. Considering the simple growth method for the structured electrode, it is impressive that the efficiency can approach that of the expensive single crystal. In Figure 3.10 and Table 3.2 are the results of the photoresponse to AM1.5 with a 385nm long pass filter. Just like the response at pH 6.4, the wire arrays produce more current at short circuit with the longer wavelength light, $44 \mu\text{A}/\text{cm}^2$ for the wires and $28 \mu\text{A}/\text{cm}^2$ for the single crystal.

Spectral Response: From Figures 3.9 and 3.10, there is a clear difference in the spectral response of the wire arrays and single crystal. In Figure 3.9, the single crystal generates slightly more current with AM 1.5 illumination, while the wires have more current with the 385 nm long pass filter. The spectral response of the single crystal and wire array at pH 11 without O_2 bubbling (the bubbling of O_2 caused too much noise in the data) measured at 5 nm intervals, Figure 3.11. Current was measured near the short circuit potential at 350 mV. The decrease in quantum

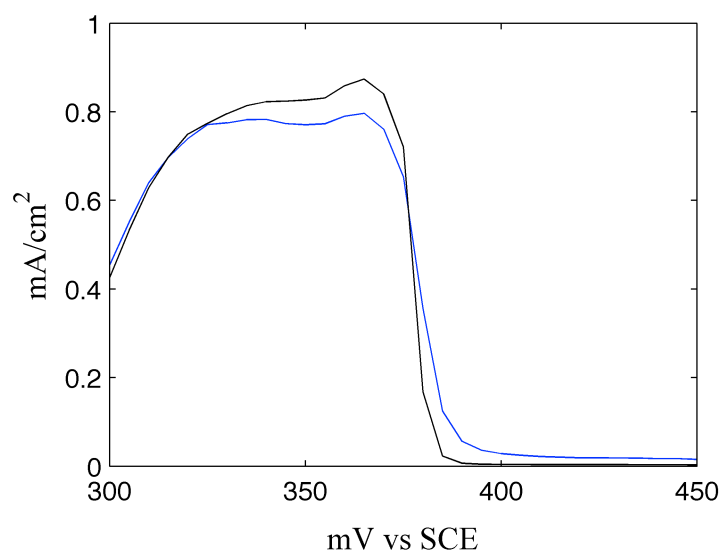


Figure 3.11: Spectral Response of the 4 μm wires (blue) and the single crystal (black) in 0.5M K_2SO_4 pH 11 no bubbling.

yield in the 300 nm to 325 nm range is due to UV absorbance by the pyrex window in the cell. Both electrodes have quantum yields exceeding 75%. The single crystal has a higher quantum yield at energies above the band gap, while at longer wavelengths the efficiency dies off more rapidly than the wire arrays. The higher quantum yield for the wires at the longer wavelengths explains the higher current with the 385 nm long pass filter for the nanowires.

The enhancement in the quantum yield at the longer wavelengths is a result of the shorter path for charge collection in the wire arrays. In the single crystal, the longer wavelengths penetrate deeper in the ZnO and have a farther distance to travel to the semiconductor – liquid junction. Any defects or traps in the semiconductor act as recombination sites and reduce the minority carrier diffusion length. Thus, as the penetration depth increases, so does the chance for recombination in the single crystal, and the quantum yield will decrease when the penetration depth is longer than the minority carrier diffusion length. In the case of the wire arrays, the charges can be collected out the sides of the wire, so even though the penetration depth increases, the distance to the junction stays the same. Therefore, the charge collection efficiency will stay the same for all wavelengths and the wires will generate more current at longer wavelengths.

3.5 Discussion

3.5.1 Affect of the Anneal

From Figure 3.5, it is clear that annealing the wires has a dramatic affect on the performance of the wire arrays, even though there is essentially no difference in

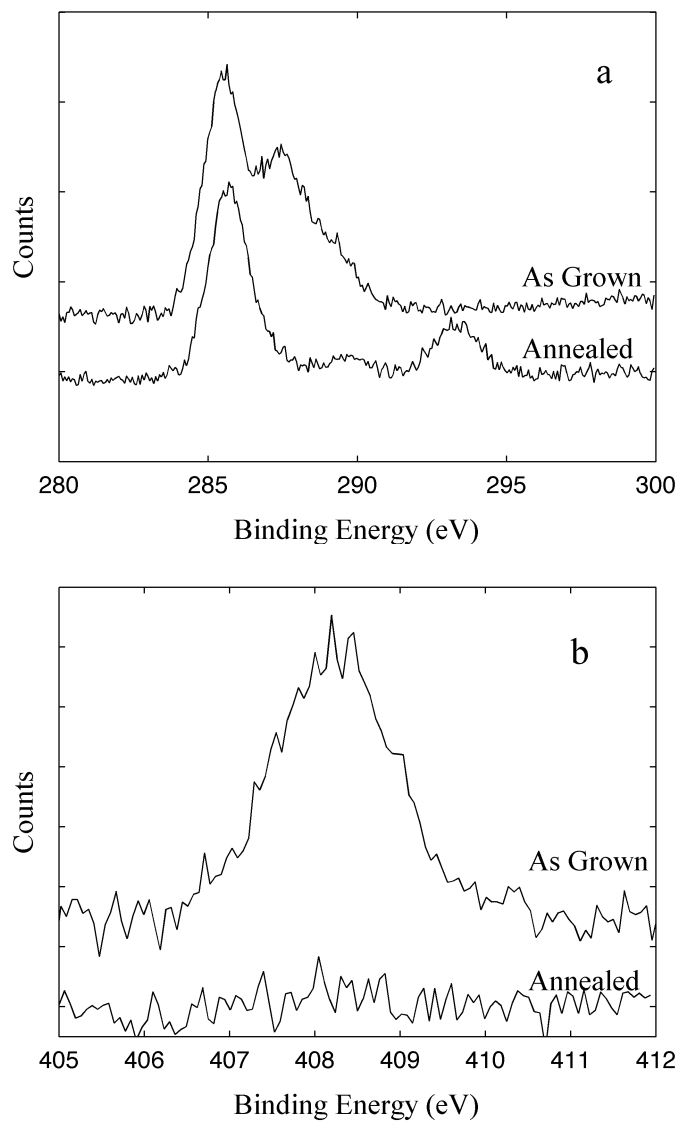


Figure 3.12: Detailed XPS scans of the carbon (a) and nitrogen (b) regions for the as grown and annealed wire arrays.

the crystalline quality, Figure 3.2. ZnO wire arrays used in dye sensitized solar cells exhibited a similar improvement after annealing the wires.²⁶ The authors hypothesized that annealing cleaned the ZnO surface of contaminants remaining from the growth solution; however, this could not be confirmed.

Using X-ray Photoelectron Spectroscopy, surface sensitive qualitative measurements examined the surface composition of the wires before and after annealing. In the growth solution, the sources of contamination are hexamethylenetetramine and nitrate, so any contaminant will contain either N or C. Detailed scans of the N 1s and the C 1s show that prior to the anneal both N and C compounds are attached to the surface, Figure 3.12. The high binding energy of the N suggests that it is in a highly oxidized state and bonded to a number of oxygen atoms. After annealing, the N peak is completely gone. In the C region, the main peak at 286 eV is due to adventitious carbon, while the shoulder at higher binding energy is the contaminant. The C peak reduces in intensity and shifts to higher binding energy after the anneal, suggesting an oxidation and removal of the C contaminant. These results are contrary TEM results, which showed no C or N contamination.¹⁰ For the samples tested in this work, it appears that annealing in air does oxidize and remove surface contamination from the growth solution. The increase in performance for water oxidation is likely due to the removal of possible surface trap states created by the contaminant or to improved kinetics with a clean surface.

3.5.2 Water Oxidation Kinetics

It is clear from the J - V curves that ZnO, as a photoanode for water oxidation, does not follow the ideal semiconductor-liquid junction behavior. The difference is at potentials near V_{oc} where the photocurrent dies off before there is any dark cathodic current. In previous studies on ZnO, single crystals in 0.5 M K_2SO_4 showed that as the current decreased near V_{oc} , the luminescence intensity increased.²² So in the region near V_{oc} , photogenerated carriers are recombining rather than crossing the interface. Furthermore, the literature values for the ZnO flat band potential, V_{fb} , have a range of -0.15 V to -0.3 V at pH 7 and therefore the bands are unbent or even slightly inverted at the V_{oc} values measured for the pH 6.4 electrolyte in Figure 3.6.^{22,27-29} Rather than the dark current overtaking the photocurrent, the photocurrent merely dies off as the bands unbend and the photogenerated carriers recombine.

Recombination occurs because the interfacial kinetics are too slow. The two rate expressions that can cause the poor interfacial kinetics are equations 3.1 and 3.4. Equation 3.4 is the transfer of holes in the valence band into solution, and if $\bar{K}_{VB} < \phi\Gamma$, then holes will accumulate at the interface resulting in an increase in recombination. In Figure 3.13, the photoresponse to varying light intensities of 365nm light is depicted. J_{sc} is linear with light intensity for the single crystal and wires arrays, Figure 3.14, indicating that the valence band kinetics are light limited and not causing recombination. This is not surprising considering the large driving force for water oxidation and high concentration of H_2O . Therefore, the slow interfacial kinetics must be from the conduction band, equation 3.1.

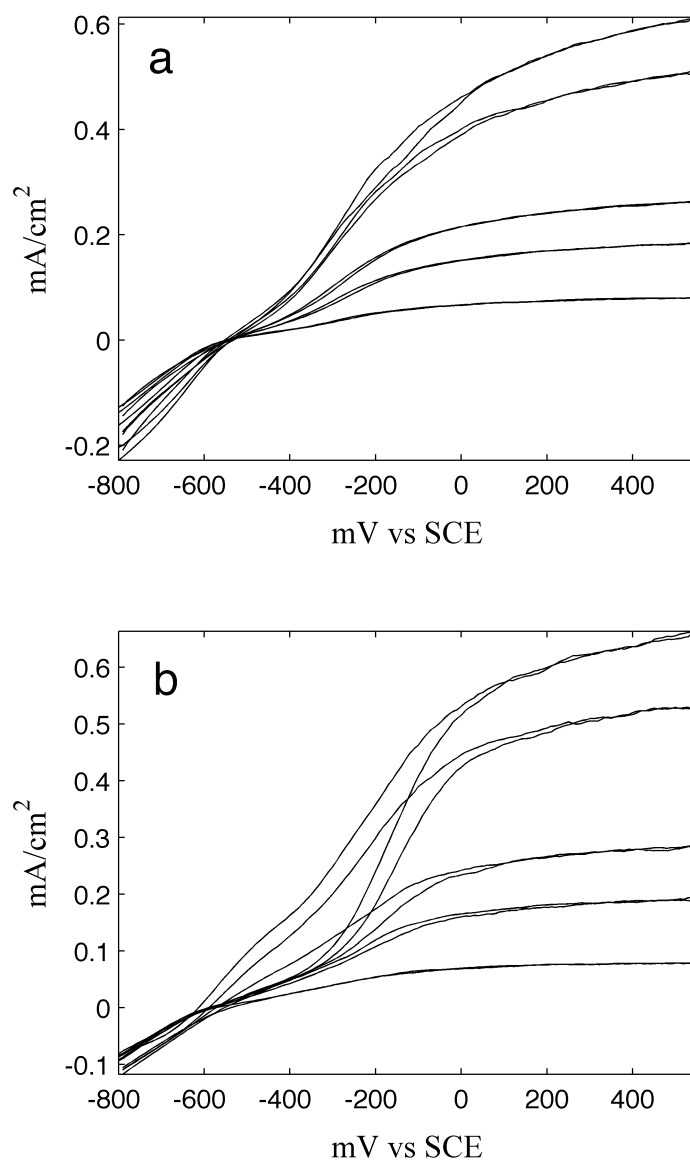


Figure 3.13: Photoresponse to 365 nm light for the $4 \mu\text{m}$ length nanowire arrays (a) and the single crystal (b). The power intensities were 3.02, 2.52, 1.26, 0.862, 0.37 mW/cm^2 .

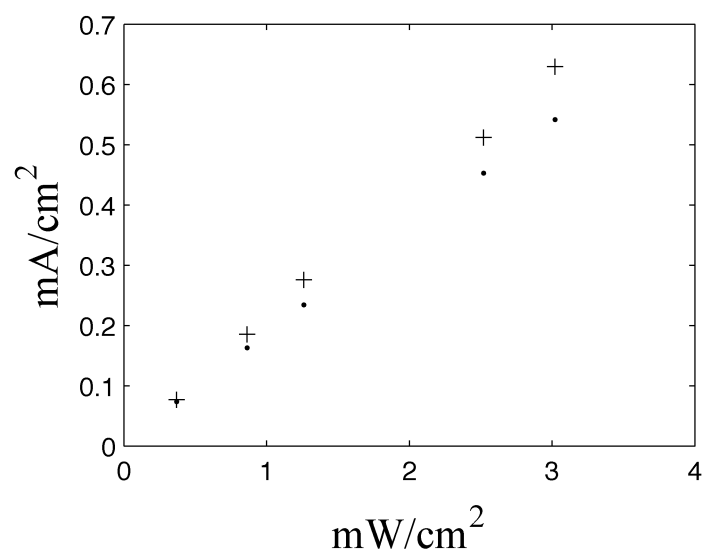


Figure 3.14: Plot of light intensity versus J_{sc} for the 4 μm length nanowire arrays (•) and the single crystal (+).

The shape of the dark currents for both electrodes in Figures 3.9 and 3.10 are indicative of low limiting currents and small rate constants for the reduction of O_2 by ZnO valence band electrons. Even for potentials past V_{oc} , the cathodic current never approaches values near J_{sc} . With essentially no cathodic current, the photoanodic current exists until the bands are unbent and the photogenerated carriers recombine. For pH 6.4 without O_2 bubbling, the O_2 concentration is only ~ 0.3 mM and has a low limiting cathodic current. Furthermore, the kinetics for O_2 reduction involves a complex multi-electron reaction and with a smaller driving force, the rate constant is likely to be small. TiO_2 single crystals generated the same type of J - V curve for water oxidation and slow O_2 reduction rates were determined to be the cause of the non-ideal curve.³⁰

From Figures 3.7 and 3.9, there is a clear difference in performance for the two different electrolytes. When the electrolyte is changed from pH 6.4 to 11 and O_2 is bubbled, the V_{oc} shifts to more negative potentials, and there is more current near V_{oc} . The shift in V_{oc} is partially due to the 59 mV per pH unit shift in the conduction band and solution potentials and an additional Nernst shift from the change in O_2 concentration. The increase in current near V_{oc} is due to the fast conduction band kinetics. With the faster kinetics the J - V curves approach a more ideal behavior.

3.5.3 Difference Between the Single Crystal and Wire Arrays

The performance of the inexpensive wet chemical synthesis wire arrays approached the efficiency of the more expensive single crystal. The high surface area samples increase the quantum efficiency at the longer wavelengths as shown in Figure 3.11; however, the high quality single crystal has a long minority carrier

diffusion length and the difference in current is minimal. ZnO single crystal diffusion lengths have been reported to be 450 nm.³¹ For wavelengths where the minority carrier diffusion length is shorter than the absorption length in planar samples, the high surface areas will generate more current. From the response of the wire arrays we can conclude that the minority carrier diffusion length is longer than the average radius of 85 nm.

Previous work on high surface area semiconductor electrodes predicts a loss in V_{oc} proportional to the surface area enhancement, λ .^{6,7} From equation 3.7, the V_{oc} is dependant on J_{ph} and J_o . When comparing the same planar area and J_{ph} , the structured electrode will have an increased area, by a factor of λ , for interaction with the solution. This increase in area will increase J_o by at least the factor of λ and V_{oc} is determined by equation 3.10.

$$V_{oc} = \frac{kT}{q} \ln\left(\frac{J_{ph}}{\lambda J_o}\right) \quad (3.10)$$

The increase in J_o is clearly evident in the dark curves from Figure 3.7 and 3.9 where in both case the wires have considerably higher dark cathodic currents. This predicts for every factor of ten increase in surface area, there is a loss of 60 mV. The surface area enhancement for a single wire with an 85 nm radius and 4 μm in length is ~ 95 . The actual surface area enhancement will be lower based on the density of wires, but a loss in V_{oc} of more than 60 mV is predicted for the wires array by equation 3.10. The observed V_{oc} for both the single crystal and wire arrays are essentially the same at pH 6.4 with a slightly more negative value for the wires. At

pH 11, the single crystal generates more voltage, but by only 36 mV, so the wire arrays did not have the predicted loss in V_{oc} .

Equation 3.10 assumes that J_{ph} is independent of voltage, but as discussed earlier, this is not the case for ZnO as a photoanode for water oxidation. Rather than the dark current overtaking J_{ph} , the photocurrent dies off as the bands unbend. In this case, V_{oc} is dependant on V_{bi} and the voltage needed to unbend the bands. V_{bi} is the difference in the Fermi level ZnO and the solution potential. With the same dopant density, the single crystal and wire arrays have the same V_{bi} and therefore, the same V_{oc} .

In order to improve the conduction band kinetics, catalysts will be needed to improve the rate constant, or the cell will need to be run under higher pressures of O_2 . These changes should result in an improved fill factor and a slight loss in V_{oc} ; however, with both values changing it is difficult to predict the overall effect on efficiency. The higher limiting cathodic currents for the nanowire arrays suggest that smaller improvements in the electron transfer rate are needed for the nanowire arrays than the single crystal. Rare earth metals like RuO have been used as catalysts for water oxidation. With the high surface area of the structured electrodes, the current densities will be smaller allowing for the use of less expensive and earth abundant materials.

3.6 References

- (1) Bard, A. J.; Fox, M. A. *Acc. Chem. Res.* **1995**, *28*, 141.
- (2) Lewis, N. S.; Nocera, D. G. *P. Natl. Acad. Sci. USA* **2006**, *103*, 15729.
- (3) Bolts, J. M.; Wrighton, M. S. *J. Phys. Chem.* **1976**, *80*, 2641.
- (4) Khaselev, O.; Turner, J. A. *Science* **1998**, *280*, 425.
- (5) Kayes, B. M.; Atwater, H. A.; Lewis, N. S. *J. Appl. Phys.* **2005**, *97*.
- (6) Maiolo, J. R.; Atwater, H. A.; Lewis, N. S. *Journal of Physical Chemistry C* **2008**, *112*, 6194.
- (7) Maiolo, J. R.; Kayes, B. M.; Filler, M. A.; Putnam, M. C.; Kelzenberg, M. D.; Atwater, H. A.; Lewis, N. S. *Journal of the American Chemical Society* **2007**, *129*, 12346.
- (8) Spurgeon, J. M.; Atwater, H. A.; Lewis, N. S. *J. Phys. Chem. C* **2008**, *112*, 6186.
- (9) Greene, L. E.; Law, M.; Goldberger, J.; Kim, F.; Johnson, J. C.; Zhang, Y. F.; Saykally, R. J.; Yang, P. D. *Angewandte Chemie-International Edition* **2003**, *42*, 3031.
- (10) Vayssieres, L. *Adv. Mater.* **2003**, *15*, 464.
- (11) Vayssieres, L.; Keis, K.; Hagfeldt, A.; Lindquist, S. E. *Chem. Mater.* **2001**, *13*, 4395.
- (12) Ahn, K. S.; Shet, S.; Deutsch, T.; Jiang, C. S.; Yan, Y. F.; Al-Jassim, M.; Turner, J. J. *Power Sources* **2008**, *176*, 387.
- (13) Yang, X.; Wolcott, A.; Wang, G.; Sobo, A.; Fitzmorris, R. C.; Qian, F.; Zhang, J. Z.; Li, Y. *Nano Lett.* **2009**, *9*, 2331.

- (14) Tan, M. X.; Laibinis, P. E.; Nguyen, S. T.; Kesselman, J. M.; Stanton, C. E.; Lewis, N. S. In *Progress in Inorganic Chemistry, Vol 41* 1994; Vol. 41, p 21.
- (15) Lyon, L. A.; Hupp, J. T. *The Journal of Physical Chemistry B* **1999**, *103*, 4623.
- (16) Hamann, T. W.; Lewis, N. S. *J. Phys. Chem. B* **2006**, *110*, 22291.
- (17) Bolts, J. M.; Wrighton, M. S. *The Journal of Physical Chemistry* **1976**, *80*, 2641.
- (18) Vayssieres, L.; Keis, K.; Lindquist, S. E.; Hagfeldt, A. *J. Phys. Chem. B* **2001**, *105*, 3350.
- (19) Webb, L. J.; Lewis, N. S. *J. Phys. Chem. B* **2003**, *107*, 5404.
- (20) Bansal, A.; Li, X. L.; Yi, S. I.; Weinberg, W. H.; Lewis, N. S. *J. Phys. Chem. B* **2001**, *105*, 10266.
- (21) Hamann, T. W.; Gstrein, F.; Brunschwig, B. S.; Lewis, N. S. *J. Am. Chem. Soc.* **2005**, *127*, 7815.
- (22) Schoenmakers, G. H.; Vanmaekelbergh, D.; Kelly, J. J. *J. Phys. Chem.* **1996**, *100*, 3215.
- (23) Bard, A. J.; Faulkner, L. R. *Electrochemical Methods : Fundamentals and Applications*; Wiley: New York, 1980.
- (24) Connor, P. A.; McQuillan, A. J. *Langmuir* **1999**, *15*, 2916.
- (25) Lefevre, G. *Adv. Colloid Interface Sci.* **2004**, *107*, 109.
- (26) Law, M.; Greene, L. E.; Johnson, J. C.; Saykally, R.; Yang, P. D. *Nature Materials* **2005**, *4*, 455.

- (27) Bohe, A. E.; Vilche, J. R.; Juttner, K.; Lorenz, W. J.; Paatsch, W. *Electrochimica Acta* **1989**, *34*, 1443.
- (28) Gerischer, H. *Electrochimica Acta* **1989**, *34*, 1005.
- (29) Hamann, T. W.; Gstrein, F.; Brunschwig, B. S.; Lewis, N. S. *Chemical Physics* **2006**, *326*, 15.
- (30) Kesselman, J. M.; Shreve, G. A.; Hoffmann, M. R.; Lewis, N. S. *Journal of Physical Chemistry* **1994**, *98*, 13385.
- (31) Lopatiuk, O.; Chernyak, L.; Osinsky, A.; Xie, J. Q.; Chow, P. P. *Appl Phys Lett* **2005**, *87*.

Chapter 4

ZnO Nanowire Arrays in Dye-Sensitized Solar Cells with Fast Redox Couples

4.1 Introduction

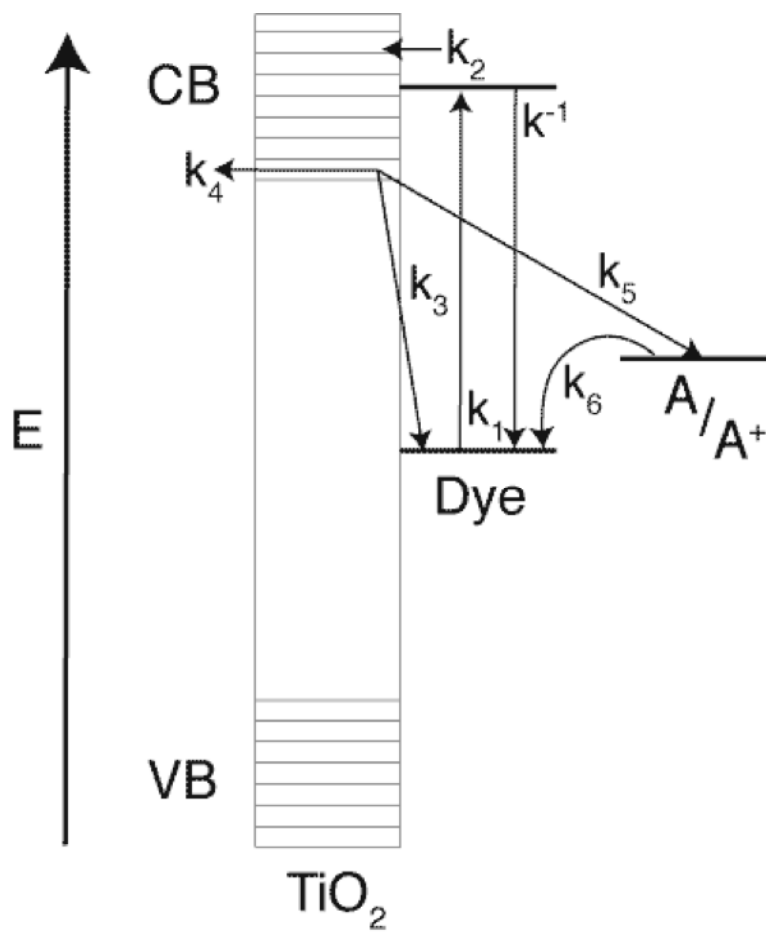
The detrimental environmental impact of burning fossil fuels has fueled research on ways to reduce the cost of solar energy conversion. Recent findings suggest that structured electrodes provide a viable means to increase the efficiency of less expensive semiconductor materials.¹⁻⁷ Structured electrodes, such as wire arrays, are able to provide a high surface area to collect charge or adsorb dye and still maintain many of the favorable properties of planar semiconductor – liquid junctions. With a sufficient diameter, the individual wires will have band bending and exhibit a rectifying behavior in a redox active solution.^{1,8-10} Furthermore, the nanowire arrays offer a more direct charge transport than other high surface area electrodes such as a nanoparticle film.^{11,12} All of these properties are advantageous to dye-sensitized solar cells (DSSC); however, not all of them have been fully utilized.

In a typical DSSC, a nanocrystalline metal oxide film is coated with a Ruthenium based dye and placed in an iodide / triiodide solution with a platinum counter electrodes. Efficiencies as high as 11% have been achieved, and the overall design could provide an inexpensive alternative to photovoltaics.¹³ Unlike

photovoltaic cells, the semiconductor is not photoactive in a DSSC and therefore, the material quality is less important because recombination does not occur within the semiconductor.¹⁴ Instead, the dye absorbs the light, and charge separation occurs by an electron being injected into the metal oxide conduction band, Scheme 4.1. Unfortunately, over the past 15 years there were only minimal improvements in the device efficiency.^{7,13,15} The problem is the lack in variability of the components involved in the DSSC.

At the working electrode of the DSSC, optimizing the current producing rates and reducing any deleterious rates is extremely important due to the high surface area of the electrode, Scheme 4.1. The current producing rates are: excitation of the dye by light, k_1 , followed by electron injection into the TiO_2 film, k_2 , the electron then diffuses through the nanocrystalline network to the back contact, k_4 , and the dye is regenerated by the redox couple in solution, k_6 . The deleterious rates are k_3 , the recombination of injected electrons to the dye and the back reaction of injected electrons to the acceptor species in solution, k_5 .

In photovoltaic devices, similar rates are controlled by the electric field at the interface.¹⁶ Unfortunately, the small particle size in the nanocrystalline film does not support a substantial electric field; therefore, the kinetics of the components directly determine the rates. For example, the redox couple needs to have slow kinetics with TiO_2 and fast regeneration rates with the dye. The I^-/I_3^- redox couple meets the requirements; however, if we wanted to change the redox couple and keep the same dye and metal oxide, the new redox couple must have essentially the



Scheme 4.1: Rates at the working electrode in a typical DSSC.

same rates as the I^-/I_3^- redox couple. This is a hefty requirement and only a few redox couples can foot the bill.^{17,18}

The small selection of redox couples severely limits the performance of the DSSC. The built-in voltage, V_{bi} , is determined by the difference in the Fermi level of the semiconductor and the solution potential. Semiconductors like TiO_2 and ZnO are the most common for DSSC and have similar Fermi levels.¹⁹ Therefore, the best way to change V_{bi} is by changing the solution potential. With a limited set of semiconductors and a limited set of redox couples, V_{bi} is essentially fixed for the nanocrystalline film design. Furthermore, only dyes that straddle this gap can be used; therefore, the maximum spectral overlap and current is fixed as well. This is the main reason that the efficiency in the DSSC has remained stagnant for the last 15 years.

With nanowire arrays, benefits like band bending can be incorporated into the DSSC. Band bending will help prevent the back reaction and allow for a wider selection of redox couples.¹⁰ Rather than relying on the slow kinetics of the redox couple, the electric field at the surface of the semiconductor will prevent the back reaction. The nanowires arrays still have a high surface area for dye bonding and allow for a further optimization of the DSSC. In this chapter, I will explore the use of ZnO nanowires arrays in DSSC with different redox couples.

4.2 Experimental Methods:

Chemicals: Zinc nitrate hexahydrate 98%, hexamethylenetetramine 98%, Ferrocene (Fc), dibromo-ferrocene (BrFc), and ferrocenium hexafluorophosphate

were purchased from Aldrich. The N719 dye, *cis*-diisothiocyanato-bis(2,2'-bipyridyl-4,4'-dicarboxylato)ruthenium(II) bis(tetrabutylammonium) was purchased from Solaronix. Ferrocene (Fc) and dibromo-ferrocene (BrFc) were purchased from Aldrich and purified by sublimation. All chemicals were reagent grade or better and used as received.

Wire Growth: ZnO nanowire arrays were grown using the method of Vayssieres with slight modifications.²⁰ A thin film of ZnO was used to seed the nanowire growth and increase the wire density. The thin film was deposited by sputtering roughly 20nm of zinc metal (RF magnetron sputterer, Zn target of 99.99% purity from Kurt J. Lesker Company) onto a fluorine doped tin oxide (FTO) slide with part of the FTO masked to be later used for electrical contact. The zinc was thermally oxidized at 400°C for 2 hours under the flow of air. After protecting the bare FTO with nail polish, the slides were placed diagonally in the aqueous growth solution with the seed layer face down. Short wires, 4 μm in length, were grown from 50 mM solution of ZnNO₃ and hexamethylenetetramine at 95°C for 4 hours followed by an additional 4 hours. Long wires, 30 μm, were grown using a continuous flow setup in 5 mM solution. The flow was such that the solution was replaced every 3 hours for a total growth time of 110 hrs. After growth, the slides were allowed to cool, rinsed with water and the nail polish was removed with acetone. Annealing the slide at 450°C for 1 hour in air improved the cell performance. Dye binding for N719 was from a 0.1mM ethanol solution for 15 minutes. CdS quantum dots were also used as sensitizers and prepared by the chemical bath technique.²¹

Photoelectrochemistry: The working electrode was prepared by gluing a copper-tin wire to the back of the slide, and silver print was used to make contact between the wire and bare FTO on the front. White epoxy encased the electrodes, and the surface area was determined by digitizing photographs of the exposed area. Photoelectrochemical measurements were done in a three-electrode pyrex cell with a platinum mesh as the counter electrode and a platinum wire at the solution potential, as the reference. The working electrode was placed within a few mm of the bottom of the cell to limit absorption by the solution and illumination was from the bottom. Four different electrolytes were used. An aqueous $\text{Fe}(\text{CN})_6^{3+} / \text{Fe}(\text{CN})_6^{2+}$ solution was made from a solution of 10 mM $\text{K}_2\text{Fe}(\text{CN})_6$ and 0.5 M K_2SO_4 . $\sim 1\text{mM}$ of $\text{Fe}(\text{CN})_6^{2+}$ was electrosynthesized at 0 V vs SCE and the final solution potential was 225 mV vs SCE. A 10 mM BrFc / 1mM BrFc⁺ was also made by electrosynthesis from a 10 mM BrFc and 0.5 M LiClO_4 solution in acetonitrile at a 200 mV applied bias. The other two electrolytes, Fc / Fc⁺ and S^{2-} / S were made by dissolving the components in solution. All electrolytes were stirred. The light source was an Oriel Inc. solar simulator, with air mass (AM) 1.5 filters and at 100mW/cm². For all dye-sensitized electrodes, a 385 nm long pass filter was used to limit the absorbance by the ZnO.

Single wire resistance measurements: The ZnO nanowires were removed from the substrate by sonicating the long wires in ethanol. The wires were spin cast on a degeneratively n-doped silicon wafer with 300 μm of thermal oxide. Using e-beam lithography, contacts were patterned on individual wires. The location and alignment of the wires was performed on the SEM and low accelerating voltages and

beam currents were used to prevent complete exposure of the PMMA. After developing the PMMA, 250 nm of Ti and 50 nm was deposited by e-beam evaporation.

4.3 Results:

4.3.1 ZnO Nanowire Electrodes

The solution grown ZnO nanowire arrays are in Figure 4.1. Both electrodes are highly crystalline as seen by the faceted wires, and the growth occurs perpendicular to the substrate. The 'short' arrays are 4 μm in length and have an average diameter of ~ 175 nm, Figure 4.1a, while the 'long' arrays have lengths of 26 μm and an average diameter of ~ 250 nm, Figure 4.1b. The surface area enhancement for the individual wires is 416 for the long wire and 91 for the short; however, the surface area enhancement for the electrode will depend on the wire density and the values will be lower.

4.3.2 Photoactive ZnO Nanowires in Aqueous $\text{Fe}(\text{CN})_6^{2+} / \text{Fe}(\text{CN})_6^{3+}$

When the wires are placed in a redox active solution, the Fermi level of the ZnO equilibrates with the solution potential and an electric field develops at the interface. For n-type semiconductors, the electric field acts as a potential barrier for electrons going into solution. Bare short nanowire arrays generate this electric field in a $\text{Fe}(\text{CN})_6^{2+} / \text{Fe}(\text{CN})_6^{3+}$ aqueous solution as indicated by the rectifying behavior of the current - voltage curve in Figure 4.2. Furthermore, under illumination the bare nanowire arrays generate reasonable currents, when considering the small

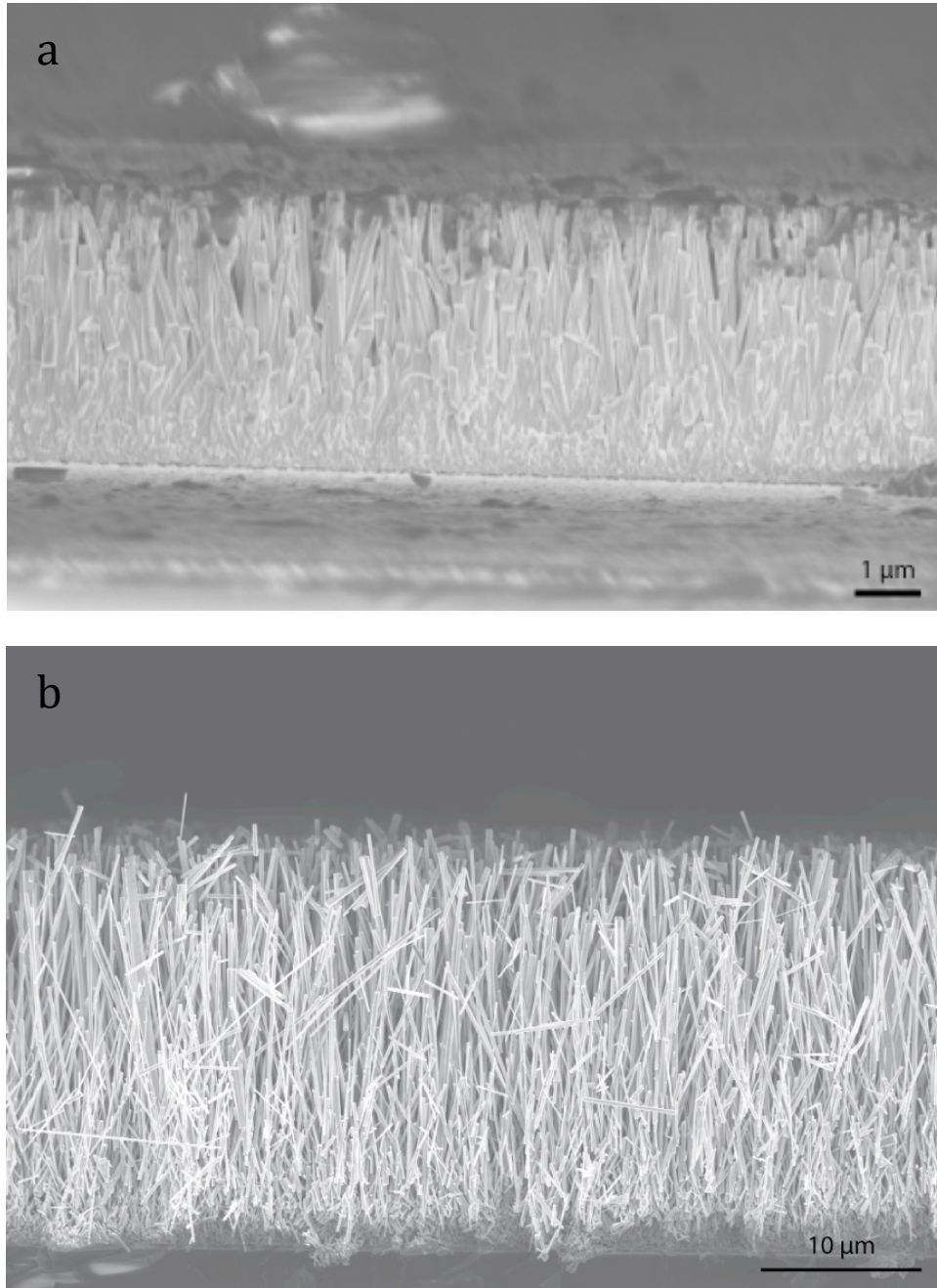


Figure 4.1: ZnO nanowire arrays grown the hydrothermal method. (a) is the short array and (b) is the long array.

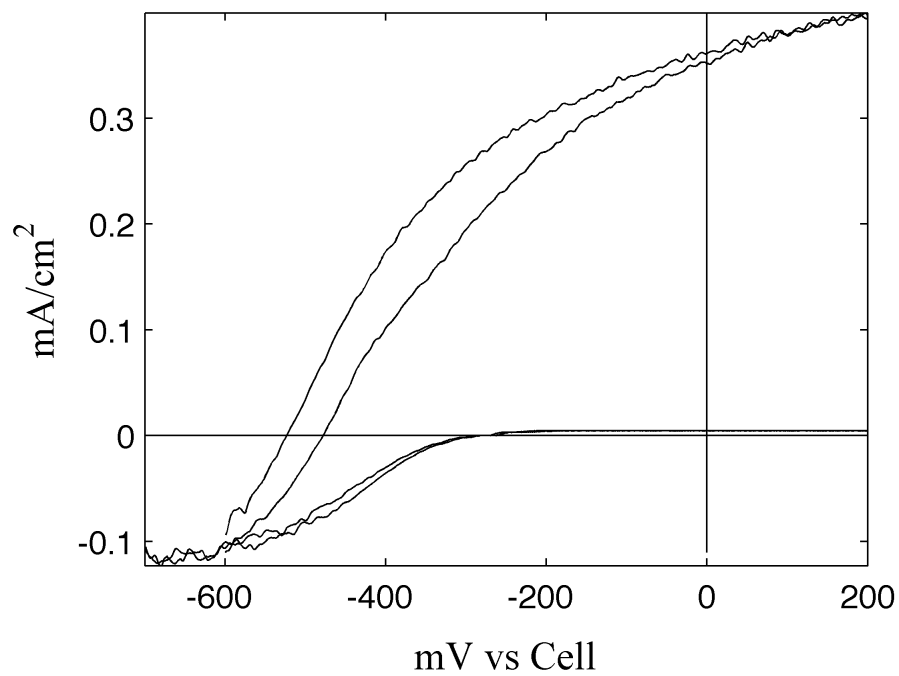


Figure 4.2: Am 1.5 light and dark responses of bare 4 μm long ZnO nanowire arrays in a 10 mM $\text{Fe}(\text{CN})_6^{2-}$ / 1 mM $\text{Fe}(\text{CN})_6^{3-}$ aqueous solution with 0.5 M K_2SO_4 .

amount of UV light with AM 1.5 conditions. Figure 4.2 clearly demonstrates that these wire arrays are able to prevent the back reaction with a fast redox couple.

4.3.3 ZnO Nanowire DSSC with Fast Redox Couple

A DSSC requires the high surface area electrode because only a monolayer of dye effectively injects photogenerated electrons into the semiconductor conduction band. The surface area enhancement of nanocrystalline films is around a factor of 1000. The surface area enhancement of the wire array is less than 416 for the long wires, so the currents will be significantly less than the nanocrystalline films. This loss in current can be reduced with longer wire arrays and by using dyes with high extinction coefficients. Another issue with dye binding to the nanowire arrays is that ZnO is etched in the binding solution; therefore, short soak times produce the most efficient DSSC.^{2,22} After a 15 min soak time in the N3 dye solution, the long nanowire arrays have a slightly purple tint.

The photoresponse of the dyed long nanowire array in an acetonitrile solution with the Fc / Fc⁺ redox couple is in Figure 4.3. Unlike the I⁻ / I₃⁻ redox couple, ferrocene has a fast outer sphere electron transfer. When nanocrystalline films use ferrocene as a redox couple, the DSSC generates essentially no current due to the increased rate of the back reaction.²³ In Figure 4.3, the electric field at the surface of the nanowire array is able to slow the back reaction and generate 1.15 mA/cm² at short circuit. Unfortunately, the cell was only able to generate an open circuit voltage, V_{oc} , of 205 mV and with the poor fill factor, ff, of 0.38. The overall conversion efficiency was low at 0.07%.

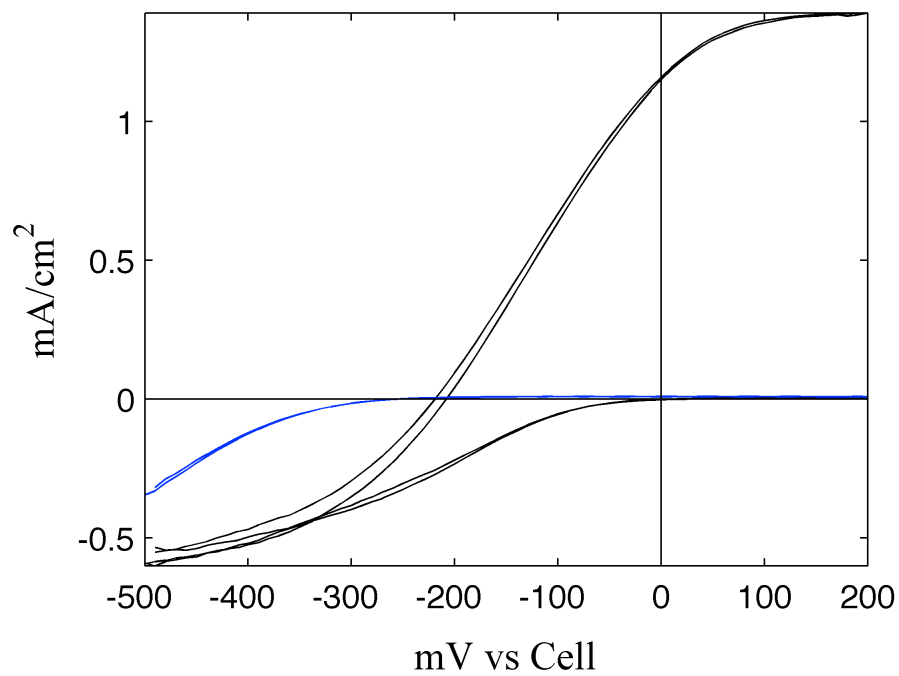


Figure 4.3: AM 1.5 with 385 nm long pass filter light and dark response of long nanowire arrays sensitized with N719 dye in 1 mM Fc / 0.1 mM Fc⁺ solution with 0.1 M LiClO₄ (black). Dark curve for the ZnO single crystal in the same solution (blue).

From the dark curve of the long nanowire array and the low V_{oc} in Figure 4.3, it is apparent that the electric field at the interface is small. ZnO nanowire DSSCs with the I^-/I_3^- generated significantly higher voltages, around 650 mV.² From Scheme 4.1, V_{bi} is determined by the difference in the Fermi level of the semiconductor and the solution potential. Considering that ferrocene and iodide have essentially the same potential, the nanowire arrays should be able to generate higher voltages. To illustrate this, dark current – voltage curves generated from single crystals in the Fc / Fc^+ solution are also shown in Figure 4.3. For the single crystal, the cathodic current does not begin until potentials of -300 mV, which will generate a higher V_{oc} . The dark current for the nanowires begins at an applied potential of only -100 mV and severely limits V_{oc} . The difference in the two dark curves is due to the increase in surface area, which predicts a shift in the dark curves by 59 mV for every factor of 10 increase in surface area.^{3,4} With a surface area enhancement less than 400 for the wires, a shift of 200 mV is higher than predicted, but is still plausible. Thus, a redox couple with a more positive redox potential is needed to generate more voltage.

Figure 4.4 displays the performance of the long nanowire array with dye in $BrFc / BrFc^+$ solution. The dark curve is shifted about 100 mV more negative than the Figure 4.3 curve, indicating the stronger electric field and slower back reaction rate. As predicted, under illumination the cell generates a larger V_{oc} of 371 mV, but at an unexpected lower current density of 0.59 mA/cm². Furthermore, the photocurrent is unstable and continually decreases with subsequent scans, Figure

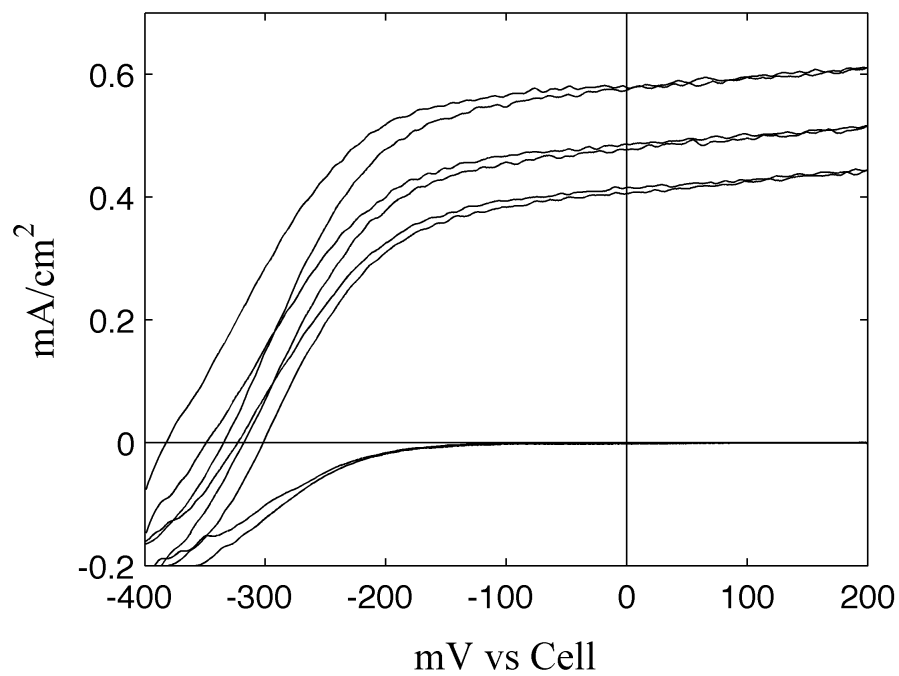


Figure 4.4: AM 1.5 with 385 nm long pass filter light and dark responses of the long wires with N719 dye in 1mM BrFc / 0.1mM BrFc⁺ in acetonitrile with 0.1 M LiClO₄. The three light curves show the decrease in efficiency for each subsequent scan.

4.4. When shifting the solution potential, the shift affects the rate of regeneration as well. There is a loss of current and the instability indicates that the regeneration rate is too slow to prevent recombination or degradation of the dye.

4.3.4 ZnO Nanowire Arrays with CdS Quantum Dots

Quantum dots, QDs, offer an attractive alternative to metal compounds, especially for electrodes with smaller surface areas. For direct band gap semiconductors, the quantum dots have higher extinction coefficients than the Ru based dyes and require less surface area for high light harvesting capabilities.²⁴ CdS has a direct band gap at 2.4 eV and the chemical bath deposition allows for an easy sensitization of the short nanowire arrays with CdS QDs.²¹ After repetitive depositions of the nanowire arrays in the Cd^+ and S^{2-} solutions, the arrays have a yellow color. The performance of the QD wire array in an S^{2-} / S aqueous solution is depicted in Figure 4.5. The QDs generate a J_{sc} of 0.89 mA/cm^2 , comparable to the current measured for the longer wire arrays with the N3 dye. Furthermore, the V_{oc} is higher at 420 mV, and with a ff of 0.37, the overall conversion efficiency is 0.13%.

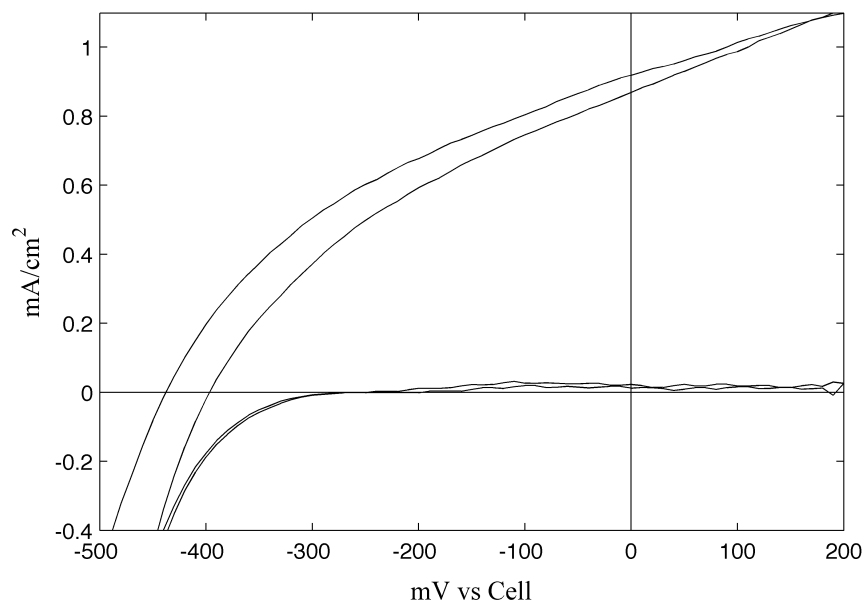


Figure 4.5: AM 1.5, with 385 nm long pass filter, light and dark response of short nanowire array sensitized with CdS quantum dots in a 0.1 M Na₂S / 0.1 M S aqueous 1 M KOH electrolyte.

4.4 Discussion

The results of the wire arrays in the DSSC demonstrate the ability to switch to fast redox couples and different dyes, but there is clearly room for improvement. Both the current and voltage need to be increased in order to match the efficiencies of the typical DSSC. For the nanowire arrays, the surface area is obviously the cause of the lower currents with the N719 dye. Nanoparticle films have a substantially higher surface area than the wire arrays used here. Fortunately, with the 'long' arrays producing 1.15 mA/cm^2 , predicts that currents matching the nanoparticle film can be obtained with reasonable wire attributes. Likewise, using sensitizers with higher extinction coefficients, for example QDs, can increase the currents as illustrated in Figure 4.5.

Increasing the voltage with the fast redox couple requires a stronger electric field at the surface of the semiconductor to prevent recombination. For the maximum amount of band bending and surface area, the radius of the wires should match the depletion width, w . The depletion width indicates how far the electric field extends into the semiconductor and is calculated by equation 5.1:

$$w = \sqrt{\frac{2\epsilon_s V_{bi}}{qN_d}} \quad (5.1)$$

where ϵ_s is the dielectric constant of the semiconductor, q is the charge on an electron, and N_d is the dopant density. N_d is determined from the conductivity, σ , of the ZnO wires by equation 5.2:

$$\sigma = qN_d\mu_e \quad (5.2)$$

where μ_e is the electron mobility.

Using e-beam lithography to pattern Ti/Au contacts, 4-point resistivity measurements showed that the wires were highly conductive with resistances of 0.2 Ωcm . This is in accordance with previous values reported for nanowires grown by chemical vapor deposition.⁹ ZnO nanowires have reported electron mobilities ranging from 13 cm^2/Vs to 75 cm^2/Vs .^{9,25} From these values, the ZnO nanowire depletion width for a V_{bi} of 800 mV is ~ 35 nm. In Figure 4.1, both the short and long wires have radii longer than the calculated depletion width, so the wires have the maximum amount of band bending. The short depletion width and the poor V_{oc} s, suggest that the electric field does not fully prevent charge recombination. With a short depletion width, the current may be tunneling through the electric field and increasing w would decrease charge recombination. w is increased by decreasing N_d and requires higher purity nanowires.

In conclusion, fast redox couples have been successfully used in the DSSC with ZnO nanowire arrays making use of the Schottky contact and the semiconductor – liquid junction. The ability to use fast redox couples in the DSSC opens a new realm of possibilities to further improve the solar energy conversion efficiency of the DSSC.

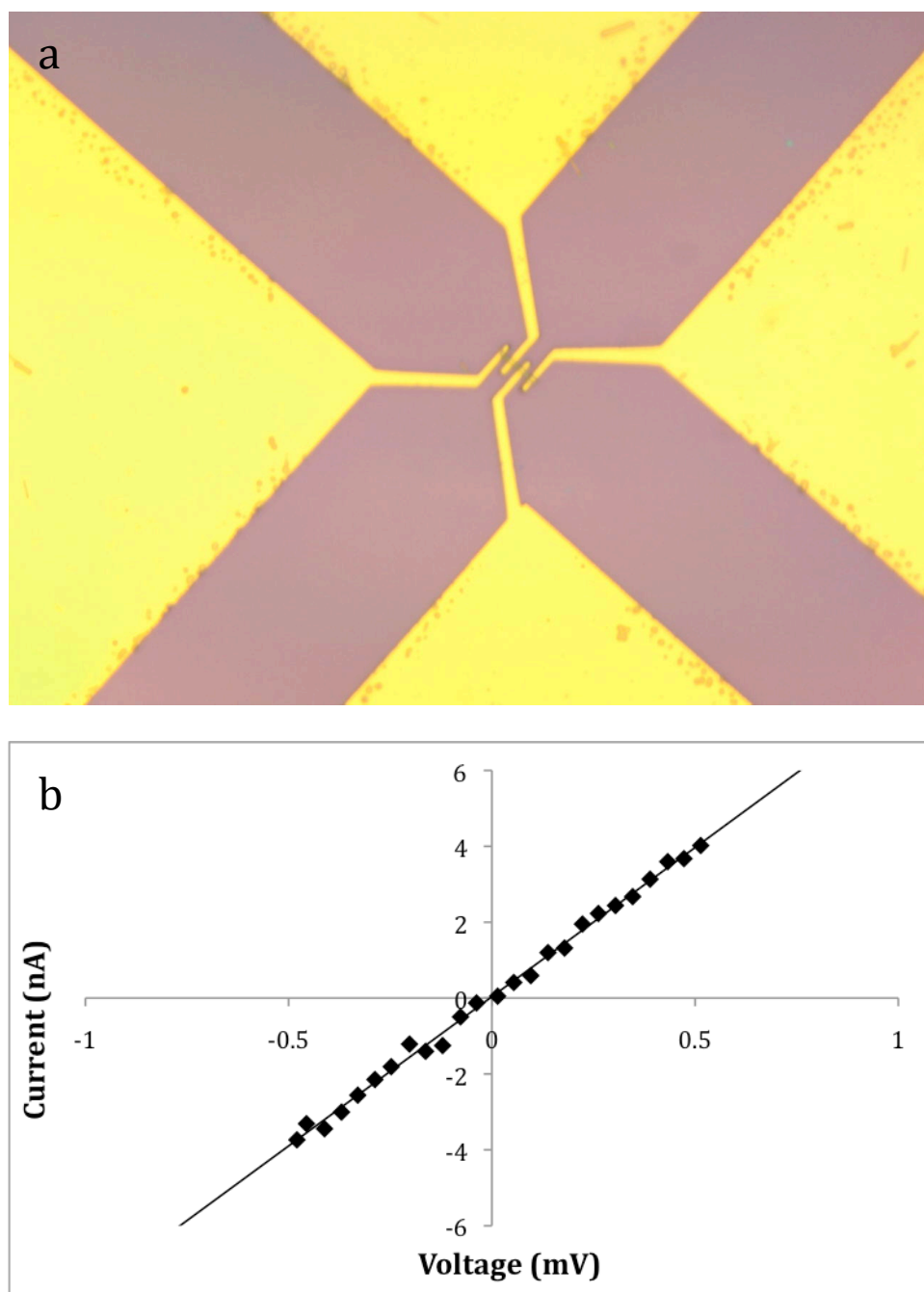


Figure 4.6: E-beam patterned Ti / Au contacts on a single ZnO nanowire (a). 4-point resistance measurements of the nanowire (b).

4.5 References

- (1) Kayes, B. M.; Atwater, H. A.; Lewis, N. S. *J. Appl. Phys.* **2005**, *97*.
- (2) Law, M.; Greene, L. E.; Johnson, J. C.; Saykally, R.; Yang, P. D. *Nature Materials* **2005**, *4*, 455.
- (3) Maiolo, J. R.; Atwater, H. A.; Lewis, N. S. *Journal of Physical Chemistry C* **2008**, *112*, 6194.
- (4) Maiolo, J. R.; Kayes, B. M.; Filler, M. A.; Putnam, M. C.; Kelzenberg, M. D.; Atwater, H. A.; Lewis, N. S. *Journal of the American Chemical Society* **2007**, *129*, 12346.
- (5) Spurgeon, J. M.; Atwater, H. A.; Lewis, N. S. *Journal of Physical Chemistry C* **2008**, *112*, 6186.
- (6) Mor, G. K.; Varghese, O. K.; Paulose, M.; Shankar, K.; Grimes, C. A. *Solar Energy Materials and Solar Cells* **2006**, *90*, 2011.
- (7) Nazeeruddin, M. K.; Kay, A.; Rodicio, I.; Humphry-Baker, R.; Mueller, E.; Liska, P.; Vlachopoulos, N.; Graetzel, M. *Journal of the American Chemical Society* **1993**, *115*, 6382.
- (8) Lu, W.; Lieber, C. M. *J. Phys. D-Appl. Phys.* **2006**, *39*, R387.
- (9) Goldberger, J.; Sirbuly, D. J.; Law, M.; Yang, P. *J. Phys. Chem. B* **2005**, *109*, 9.
- (10) Chen, Z. H.; Tang, Y. B.; Liu, C. P.; Leung, Y. H.; Yuan, G. D.; Chen, L. M.; Wang, Y. Q.; Bello, I.; Zapien, J. A.; Zhang, W. J.; Lee, C. S.; Lee, S. T. *Journal of Physical Chemistry C* **2009**, *113*, 13433.
- (11) Ku, C. H.; Wu, J. *J. Appl Phys Lett* **2007**, *91*.

- (12) Baxter, J. B.; Schmittenmaer, C. A. *J. Phys. Chem. B* **2006**, *110*, 25229.
- (13) Nazeeruddin, M. K.; De Angelis, F.; Fantacci, S.; Selloni, A.; Viscardi, G.; Liska, P.; Ito, S.; Takeru, B.; Gratzel, M. G. *Journal of the American Chemical Society* **2005**, *127*, 16835.
- (14) Gratzel, M. *Inorganic Chemistry* **2005**, *44*, 6841.
- (15) Oregan, B.; Gratzel, M. *Nature* **1991**, *353*, 737.
- (16) Tan, M. X.; Laibinis, P. E.; Nguyen, S. T.; Kesselman, J. M.; Stanton, C. E.; Lewis, N. S. In *Progress in Inorganic Chemistry, Vol 41* 1994; Vol. 41, p 21.
- (17) Oskam, G.; Bergeron, B. V.; Meyer, G. J.; Searson, P. C. *Journal of Physical Chemistry B* **2001**, *105*, 6867.
- (18) Desilvestro, J.; Gratzel, M.; Kavan, L.; Moser, J.; Augustynski, J. *J Am Chem Soc* **1985**, *107*, 2988.
- (19) Xu, Y.; Schoonen, M. A. A. *American Mineralogist* **2000**, *85*, 543.
- (20) Vayssieres, L.; Keis, K.; Lindquist, S. E.; Hagfeldt, A. *J. Phys. Chem. B* **2001**, *105*, 3350.
- (21) Sun, W. T.; Yu, Y.; Pan, H. Y.; Gao, X. F.; Chen, Q.; Peng, L. M. *Journal of the American Chemical Society* **2008**, *130*, 1124.
- (22) Baxter, J. B.; Walker, A. M.; van Ommering, K.; Aydil, E. S. *Nanotechnology* **2006**, *17*, S304.
- (23) Gregg, B. A.; Pichot, F.; Ferrere, S.; Fields, C. L. *J. Phys. Chem. B* **2001**, *105*, 1422.

(24) Lee, H. J.; Yum, J. H.; Leventis, H. C.; Zakeeruddin, S. M.; Haque, S. A.; Chen, P.; Seok, S. I.; Grazel, M.; Nazeeruddin, M. K. *Journal of Physical Chemistry C* **2008**, *112*, 11600.

(25) Park, W. I.; Kim, J. S.; Yi, G. C.; Bae, M. H.; Lee, H. J. *Appl Phys Lett* **2004**, *85*, 5052.